Optical Response of Magnetically Actuated Biocompatible Membranes

Hélène Joisten, Alain Truong, Svetlana Ponomareva, Cécile Naud, Robert Morel, Yanxia Hou, Isabelle Joumard, Stéphane Auffret, Philippe Sabon, Bernard Dieny

Optical response of magnetically actuated biocompatible membranes

H. Joisten,*[a,c] A. Truong,[a] S. Ponomareva,[a] C. Naud,[a] R. Morel,[a] Y. Hou,[b] I. Joumard,[a] S. Auffret,[a] P. Sabon[a] and B. Dieny[a]

Biocompatible suspended magneto-elastic membranes were prepared. They consist of PDMS (polydi-methylsiloxane) films, with embedded arrays of micrometric magnetic pillars made with lithography tech-niques. For visible light wavelengths, our membranes constitute magnetically tunable optical diffraction gratings, in transmission and reflection. The optical response has been quantitatively correlated with membrane structure and deformation, through optical and magneto-mechanical models. In contrast to the case of planar membranes, the diffraction patterns measured in reflection and transmission vary very differently upon magnetic field application. Indeed, the reflected beam is largely affected by the mem-brane bending, whereas the transmitted beam remains almost unchanged. In reflection, even weak mem-brane deformation can produce significant changes of the diffraction patterns. This field-controlled optical response may be used in adaptive optical applications, photonic devices, and for biological applications.

Introduction

The concept of physical membrane refers to thin films having a certain flexibility. Artificial membranes are far less complex than biological ones, which remain incomparable as inherent components of any life form,[1] and have been more and more explored for various applications in the physical world. Moreover, they may be intended to interact with biology, for understanding the functioning of cells and living organisms, or acting on them with therapeutic purposes.[2] In particular, numerous studies refer to membranes constituted of polydimethylsiloxane (PDMS) matrices, a polymer used for decades for its tunable elastic modulus.[3] The PDMS polymer is moreover biocompatible, and highly cited as a biomaterial relevant for its mechanical properties.[4,5] Likewise highly transparent, PDMS membranes may be good candidates for flexible photonic devices, the optical and mechanical properties being merged for instance in elastomeric lenses.[6] Furthermore, the contribution of micro-nanotechnology enables the fabrication of micro-nanostructured PDMS devices with various types of implementations and actuation schemes, keeping in mind the PDMS biocompatibility for biological applications,[7,8] for instance as biomimetic microsystems[9] or microfluidics devices.[10,11]

Ultrasound waves and pneumatic, capacitive, and electrostatic actuation are among the main methods explored for the actuation of synthetic membranes. Another alternative, used in this study, is magnetic actuation. More precisely, the great potential of elastic membranes embedded with magnetic particles lies in their ability to be remotely actuable by an external magnetic field. The use of magnetic micro- and nano-particles, pillars, disks or cantilevers embedded in a flexible membrane (*e.g.* PDMS membrane) constitutes a very efficient option for producing actuable flexible membranes.[12–19]

Instead of particles, permalloy multilayers nm-to-μm thick can exhibit similar properties when deposited on large areas of flexible substrates such as polyester, kapton,[20,21] polyimides,[21] and cyclo olefin copolymer, studied for instance for high-frequency sensor application.[22] These recent investigations[21–23] are however not oriented towards a mechanical actuation through the magnetic layers. Conversely, for a membrane actuation, using separate magnetic particles/pillars instead of continuous layers constitutes an important difference in terms of membrane deformability, the flexible substrate being free to bend with its own elasticity between the particles. Compared to the latter polymeric substrates, PDMS has the advantages of elasticity which can be varied in a wide range by adjusting its composition, its transparency useful for optical applications, and its quasi-non-toxicity if biological applications are targeted.

Magnetic-field-sensitive gels called ferrogels[24–26] likewise constitute a class of materials, mixing polymers and magnetic par-

[a]*Univ. Grenoble Alpes, CEA, CNRS, IRIG-SPINTEC, 38000 Grenoble, France. E-mail: helene.joisten@cea.fr*

[b]*Univ. Grenoble Alpes, CEA, CNRS, IRIG-SYMMES, 38000 Grenoble, France*

[c]*Univ. Grenoble Alpes, CEA, LETI, 38000 Grenoble, France*

Supplementary information at the end of the paper.

ticles with a direct coupling between magnetic and elastic properties,[27] with the advantage of being potentially fabricated in large quantities. Although fabricated from stable colloidal suspensions of non-agglomerated magnetic particles, the particles have to be of sufficiently small dimensions (<50 nm), and their uncontrolled random spatial distributions do not give rise to optical applications using diffraction/interference phenomena.

On the one hand, biomedical applications (such as, for instance, cancer cell destruction induced by magneto-mechanical vibrations) use the same type of magnetic particles, although dispersed in solutions *e.g.* (i) iron oxide nanoparticles produced by chemical approaches[28,29] or (ii) magnetic particles prepared by lithography techniques, in particular magnetic vortex particles.[30–33] On the other hand, arrays of magnetic particles and in particular of magnetic vortex particles are investigated in the context of data storage or spintronics applications.[34,35] Magnetic particles inserted in soft matrices at the micro- or nanoscale have already been explored for the fabrication of microswimmers[36,37] or microscale pumps.[38] Hinged anisotropic vortex particles enabled the fabrication of magnetically actuable nanotweezer arrays.[39] Besides, magneto-active PDMS substrates embedded with magnetic pillars have been investigated for their potential action on cells in culture.[40]

Likewise, remotely actuable magnetic membranes can be of interest in the broad area of photonic devices. In the photonic domain, adaptive optics,[6,41] in particular diffraction gratings with adaptable properties, are of particularly great interest. They are currently used for instance with piezo[42] or capacitive actuation.[43] Deformable and flexible diffraction gratings, in particular on PDMS-based substrates, using fluidic or pneumatic actuation in optofluidic devices,[44–46] or by mechanical stretching,[47] are studied for their tunable optical properties. Biomimetic devices, consisting of bioinspired micrograting arrays, have been likewise inspired by natural diffraction gratings.[48] Magnetic-field-sensitive diffraction gratings were similarly developed, based on arrays of flexible magnetic microcantilevers as a magnetic field mapping system.[49] The two main non-contact actuation approaches: (i) capacitive/electrostatic methods (forces from an electric field) and (ii) (electro)magnetic methods (forces from a magnetic field) were explicitly compared.[50–52] The magnetic approach provides the advantage of larger forces and displacements at long range with much smaller actuation voltages.[53] In contrast, the electrostatic approach is definitely more powerful at short distance, and is preferable for its ease of integration with CMOS technology and its fast response time, although vulnerable to breakdowns/pull-in instabilities and electrostatic discharge.[54] A distance threshold separates the preferred actuation approach (electrostatic *versus* magnetostatic) which was estimated at around 1.75 μm in ref. 55, through energy density comparisons.[50,55] Hence, magnetic actuation *via* permanent magnets is more efficient for long-range actuation – by properly adjusting the magnet size,[53] with the advantage of being able to maintain a static position without energy consumption. This approach is potentially usable in a liquid environment *e.g.* in biology. Regarding adaptive optics, the performance in terms of the vibration frequency of an elastic membrane is limited by the mechanical properties of the system; thus optical fiber modulators and data transmission requiring tens of GHz should not be envisaged for systems based on macro-/micro-membranes. Conversely, adaptive/regulating optics studies already explored the potential of deformable magnetic reflective membranes (mirrors), using independent magnetic actuators, *e.g.* for vision (ophthalmic)[56] and astrophysics[53,57] applications. Adaptive liquid or wetting lenses or micro-lenses, based on dielectric elastomer actuators,[58] stimuli-responsive hydrogel,[59] ferrofluid,[60] chemical methods or bioinspired systems,[61] constitute a large variety of lens types studied in the adaptive optics area. The present approach is inspired by the principle of a tunable magnetic membrane, as previously investigated in ref. 53 and 57.

In this context, we present here the development and characterization of a microstructured suspended magneto-elastic membrane (MEM), involving internal dimensions at micrometric or nanometric scales, and its magnetic actuation. Prepared by a top down approach, our MEMs consist of PDMS films with embedded arrays of micrometric magnetic pillars. They constitute a particular form of metamaterials, which may address needs in biology and biomedical fields, as well as in adaptive optics. Owing to the micrometric pitch of the pillar array, close to the visible light wavelengths, and the transparency of PDMS, such membranes constitute nice magnetically tunable optical diffraction gratings, in transmission and reflection. The membrane deformation under an external magnetic field and the corresponding variations in the diffraction patterns have been experimentally and theoretically studied. The paper first describes the membranes fabrication, then their magnetic properties and deformation under a magnetic field. Finally their optical response is discussed from experimental and theoretical points of view.

Results and discussion

The suspended magneto-elastic membranes, prepared as described below and detailed in the Experimental section of ESI 1,† were tested by a set of optical measurements. Step by step (i) the membrane magnetic properties, (ii) the determination of the magnetic field amplitude and gradient applied on the membrane by the used permanent magnet, (iii) the resulting magnetic forces exerted on the membrane, (iv) the determination of the corresponding elastic membrane deformations, and (v) finally, the optical responses to magnetic actuation when the membrane is illuminated by a laser beam have been addressed. In particular, the relationships between membrane deformations – sketched in Fig. 1(a)–(b) – and optical diffraction patterns have been studied in reflected and transmitted configurations. These two configurations have revealed very different behaviors as explained further.

Magneto-elastic membrane fabrication and imaging

The fabricated membranes were prepared by a top down approach. They consist of PDMS films with embedded arrays

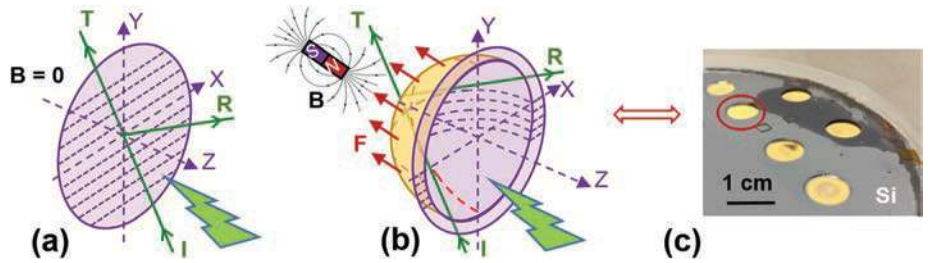

Fig. 1 Schematic principle of magneto-elastic membrane actuation, enlightened by a laser beam: incident (I), reflected (R), transmitted (T) beams, and photo of several fabricated suspended membranes, at the centimetric scale, on a 4'' silicon wafer. (a) In zero field: the membrane remains planar; the magnetic array is sketched by dashed lines. (b) In an applied magnetic field *B* exerting a pulling force, the membrane becomes concave; the magnetic array is deformed. (c) Fabricated suspended membranes on their silicon substrate. Using back side deep-etching (DRIE), the silicon wafer on which the membrane was fabricated was locally etched through, thus resulting in circular apertures covered by the suspended membranes of diameter 8 mm; the yellow color of the membranes is due to a 100 nm Au layer remaining attached to the PDMS layer.

of micrometric magnetic pillars coated with a 100 nm thick gold layer. The membranes are suspended over cylindrical apertures created in silicon substrates. The suspended membranes characterized in this study (see Fig. 1(c)) have a diameter of 8 mm and a thickness of a few micrometers (~5 μm). The polymer used for fabricating the membranes was PDMS having a Young's modulus of around 1.5 MPa (PDMS Sylgard 184, with a curing agent to monomer ratio of 1 : 10). Alternatively, as presented in ref. 3, a large range of elasticity could be further explored by adjusting the composition of PDMS in mixtures of two different compositions (Sylgard 527 and Sylgard 184). The employed Sylgard 184 is the most robust, however less flexible, composition. The tradeoff between membrane flexibility and robustness can be adjusted depending on the foreseen application.

The magnetic component embedded within the membrane consists of an array of magnetic dots, regularly distributed in its plane. They are composed here of permalloy, *i.e.* of magnetic nickel–iron alloy $Ni_{80}Fe_{20}$. The magnetic dots may be shaped in the form of pillars with adjustable aspect ratios from flat particles such as disks to vertically elongated cylinders. The cylinders lay in arrays parallel to the membrane *XY* plane, with their OZ axis perpendicular to the membrane plane.

The surface dimensions, shapes and spacing can be arbitrarily chosen, defined when designing the lithography mask. Two types of geometries have been designed: square and hexagonal arrays, each of them with various magnetic pillar diameters. Moreover, some arrays mix pillars of different diameters for testing the potential impact of two different coercivities. For remaining in the standard limits of optical lithography, the areal dimensions have been held in the micron range (≥1 μm). The permalloy has been deposited using a pulsed electrodeposition technique. In practice, permalloy is a well-known material,[62–65] currently deposited by various methods on a large variety of substrates, notably by electrodeposition (*e.g.* for flux concentrators in magnetic sensors, shields in magnetoresistive heads, flux guides in transformers...). The aim here was to be able to deposit sufficiently thick magnetic pillars, for a given membrane elasticity. Various thicknesses of permalloy have been tested between 1 and 4 μm, pillar diameters varying between 1 and 4 μm. An example of long-shaped 4 μm-thick quasi-cylindrical pillars is imaged in Fig. 2(a). The potential membrane deformation is directly related to the magnetic volume deposited. Furthermore, a 100 nm gold layer had to be deposited as the first layer on the silicon substrate for the electrical contact required in electrodeposition. Permalloy thicknesses have been finally slightly reduced, as presented below, enabling (i) easier serial fabrication, while still maintaining magnetic actuation, and (ii) electrodeposition to be replaced by techniques of evaporation or physical sputtering, which avoid the electrically conducting coating and chemical bath environment. As long as electrodeposition is used to prepare the NiFe pillars, the suspended PDMS membrane remains coated with the conducting gold layer on one of its faces. This Au coating plays a significant or even major role in limiting the membrane deformation and has definitely to be taken into account in the mechanical modelling of the membrane deformation.

Summarized in Fig. 2(b), the process involves lithography, spin-coating, and electrodeposition steps, ending with the membrane partially released through a Deep Reactive Ion Etching (DRIE) technique on the back side of the silicon substrate. The DRIE step, which consists of etching a window throughout the silicon wafer (~525 μm thick) till reaching the gold layer, turned out to be challenging (see Experimental section in ESI 1†). Finally, the process has allowed the suspension of magnetoelastic membranes 8 mm in diameter as can be seen for instance in Fig. 1(c). This back side process could be replaced by a sacrificial layer on the front side of the Si wafer, such as for instance a PMMA (poly(methyl methacrylate)) layer soluble in acetone. However, such a PMMA underlayer dissolution could be difficult considering the Au layer presence required by the electrodeposition step. Moreover, the membrane would have to be reported and bonded on a support such as a ring, before or after its release from the substrate. Conversely, the back side technique chosen here allowed a serial production of identical membranes immediately suspended in their thin hollow Si support, in a shape adapted to the present optical study. The mechanical resis-

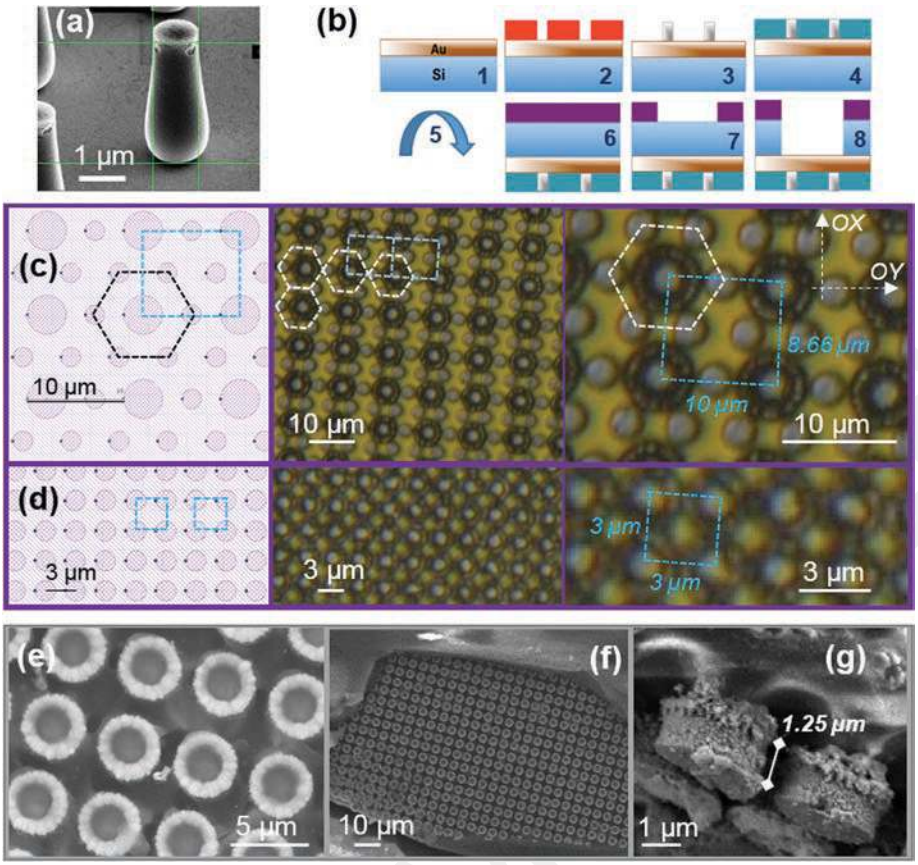

Fig. 2 The fabrication process scheme and microscopy imaging of magneto-elastic membranes. (a) SEM image of a magnetic $Ni_{80}Fe_{20}$ pillar obtained by electrodeposition (~4 μm thick, ~1 μm-diameter). (b) Flowchart of the process to fabricate arrays of permalloy pillars embedded in PDMS: (1) 100 nm Au deposited by evaporation. (2) Template patterned using UV lithography with AR 4400 thick negative photoresist. (3) $Ni_{80}Fe_{20}$ pillars grown by electrochemical deposition (ECD). (4) 5 μm-thick PDMS layer spin-coating. (5) Silicon wafer reversed. (6)–(7) Lithography on the wafer backside. (8) DRIE, till membrane release. (c–d) Optical microscopy of membranes embedding various magnetic arrays, seen through the transparent PDMS: mask patterns, membrane images and zooms. (c) Example of membrane comprising both a rectangular array of large pillars and a hexagonal one of smaller pillars; the unit cell is composed of pillars of radii: 1 × (R = 2 μm) + 3 × (R = 1 μm). (d) Example of a membrane with a square array of 3 μm × 3 μm pitches, 2 μm diameter. (e–g) SEM images of the PDMS membrane, embedding 3 μm-diameter $Ni_{80}Fe_{20}$ pillars, in square array with a pitch of 5 μm. (e) Permalloy pillars in top view. (f) PDMS layer partially present, partially removed, revealing the permalloy pillars. (g) Side view revealing ~1.25 μm thick magnetic pillars.

tance of these suspended membranes was sufficient to perform the magneto-optical tests. Reflectometry and relevant SEM (Scanning Electron Microscope) imaging confirmed the PDMS thickness of ~5 μm, as expected.

Clear images of the magnetic arrays embedded in PDMS membranes have been obtained using optical microscopy, as illustrated in Fig. 2(c–d), thanks to the PDMS transparency. For SEM microscopy, as shown in Fig. 2(e–g), PDMS layers have been removed. Top views of the magnetic arrays indicate that the magnetic pillars' size and pitch conformed to the expected ones defined by the lithography mask patterns. However, the presence of rings can be observed on the largest magnetic pillars, as shown in Fig. 2(c)–(e). A zoomed in section shows that the smaller pillars patterned in a hexagonal array came out nicely. The rings that cover the large magnetic pillars are made of $Ni_{80}Fe_{20}$ that overgrew on these pillars. Indeed, in some cases, the electrochemical deposition (ECD) seems to exhibit a faster rate at the edges of the pillars than at their center. This can be in particular the case when some photoresist still remains at the center of the circular patterns corresponding to the pillars. As a result, the ECD starts at the edge of the cylinders. The deposited metallic permalloy gradually coats the whole cylinder bottom so that the ECD finally takes place over the whole cylinder area but starts with a delay at the center. In the present study, all the hexagonal membranes comprise a rectangular array of dark cylindrical pillars of enhanced visibility compared to the surrounding small pillar hexagonal array. Both membranes of Fig. 2(c)–(e) comprise thus a visible rectangular or square array of pillars, playing a predominant role in the optical experiments, as presented below.

The NiFe pillar thickness was adjusted in the range 1–3 μm. Its value was determined from VSM (Vibrating Sample Magnetometer) measurements, and confirmed using SEM imaging, as explained further.

Magnetic properties of pillar arrays, experiment

The magnetic properties of the $Ni_{80}Fe_{20}$ pillar arrays were investigated using VSM, by measuring their magnetic moment $\mu_0 M$ *versus* applied magnetic field $\mu_0 H$, (vacuum permeability constant $\mu_0 = 4\pi \times 10^{-7}$ H m^{-1}). For these measurements, the silicon wafer was only partially etched so that the membranes remain flat and inflexible during the VSM measurements, in contrast to magneto-active elastomers.[66] The magnetic moments have been measured with the field applied in-plane (IP) and out-of-plane (OOP). One goal was to express the magnetic force F_Z exerted by a permanent magnet along the OZ axis (OOP), on a similar but suspended and flexible neighboring membrane, and the resulting elastic deformation. Both IP and OOP hysteresis loops are required beforehand for evaluating the magnetic state of the NiFe pillars.

Permalloy thickness L_Z was first extracted from the non-normalized hysteresis loops. The $Ni_{80}Fe_{20}$ saturation magnetization M_S is assumed to be equal to its bulk value $\mu_0 M_S = 1$ T (10^4 Gauss in CGS). A sample imaged in Fig. 2(e–g), of volume $V = 0.35$ cm × 0.5 cm × Lz, with 3 μm diameter pillars in an array of 5 μm × 5 μm pitches bears ~7×10^5 NiFe pillars and yields 5 memu at saturation [emu = $4\pi M$(Gauss) × V(cm^3)/4π in CGS]. The NiFe thickness is hence evaluated at $L_Z = 1.25$ μm, corroborated by SEM profile views, shown in Fig. 2(g). As will be shown further, this thickness is sufficient for actuating magneto-elastic membranes investigated in the optical set-up, using an NdFeB magnet. Such L_Z has thus been used in the rest of the study.

Hysteresis loops and their derivatives partly reveal the NiFe pillars' magnetic state. Normalized IP and OOP hysteresis loops shown in Fig. 3(a), and OOP zoomed in Fig. 3(b), correspond to the samples imaged in Fig. 2(e–g). The experimental OOP and IP curves are plotted respectively in black and blue colors. Superimposed green dots on the OOP experimental curve in Fig. 3(b) outline the upper hysteresis branch, H varying from H_{max} to $-H_{max}$. From the experimental curves, the magnetic susceptibilities have been derived: (1) the OOP differential susceptibility dM/dH plotted in Fig. 3(c) as a function of $\mu_0 H$ and (2) the IP initial susceptibility $\chi(0)$ *versus* pillar aspect ratio, Fig. 3(d).

As a first observation in Fig. 3(a), the OOP loop is more slanted than the IP one. This indicates an in-plane anisotropy, in agreement with the shape anisotropy of the magnetic pillars (cylinder radius $R = 1.5$ μm in XY plane, thickness $L_Z = 1.25$ μm on the OZ axis). The shape anisotropy is clearly the dominant anisotropy here since magnetocrystalline anisotropy is known to be weak in permalloy.[69] Besides, the sample was prepared without any field-induced-magnetic anisotropy, field-annealing treatment, or field applied during electrodeposition, thus without any induced magnetic anisotropy which could exceed the shape anisotropy.[70] Considering the geometry of the used NiFe pillars, their ground magnetic states are likely in a vortex[36–47] for several reasons: (i) the aspect ratios $\beta = L_Z/R$[68]

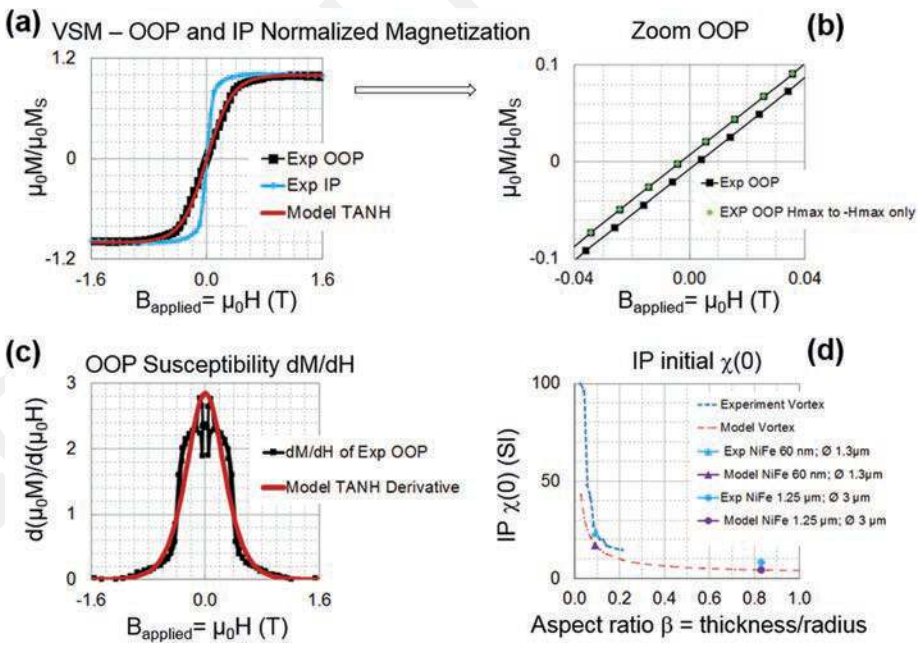

Fig. 3 Magnetic membrane characterization: VSM measurements and fitting models; square permalloy arrays of pitches 5 μm × 5 μm, pillar diameter 3 μm, thickness $L_Z \sim 1.25$ μm. (a) Experimental OOP (black color) and IP (blue color) hysteresis loops. Phenomenological model fitting the OOP loop (red color): $\mu_0 M(\mu_0 \cdot H) = \tanh(k \cdot \mu_0 \cdot H)$, with $k = 55$; (b) zoom: OOP experiment in black color; superimposed upper branch, in green color: H_{max} to $-H_{max}$. (c) OOP differential susceptibility dM/dH, calculated on (i) experimental loop (background black color), (ii) derivative of the TANH model (red color); compromise for fitting the slope near $\mu_0 H \sim 0.5$ T and around 0, keeping experimentally largest values near 0. (d) IP initial susceptibility $\chi(0)$ *versus* pillar aspect ratio $\beta = L_Z/R$: (i) a large blue round dot for the present NiFe pillars ∅ 3 μm, 1.25 μm-thick imaged in Fig. 2(e–g), $\beta = 0.83$; and (ii) a large blue triangle dot from recent NiFe pillar array, ∅ 1.3 μm, 60 nm-thick, $\beta = 0.09$; fitting previous IP magnetic vortex curves.[67,68]

are below the limit of an OOP shape anisotropy; (ii) the NiFe cylinders' circular shapes and diameters are below the limit of multidomain structures;[71,72] and (iii) according to phase diagrams mapping the magnetic ground states of cylindrical dots,[73–75] for the sizes of our NiFe pillars, the vortex state should be the most stable one. Noticeably, in each pillar, the magnetization of the upper ring described above may be coupled with the cylinder one, thereby reinforcing the trend towards vortex formation.[76]

Concerning the variation of the IP initial susceptibility $\chi(0)$ *versus* aspect ratio β, the experimental data can be fitted by the analytical model of Guslienko *et al.*, 2001[68] (Fig. 3(d)). In this model, the IP initial susceptibility is given by $\chi^{-1}(0) = 2\beta \times [\ln(8/\beta) - 1/2]$ in CGS units, $\chi(0) \times 4\pi$ in SI units. A slight increase of $\chi(0)$ above theoretical expectations, already observed in an earlier study on arrays of vortices,[67] is also observed here. It may result from an IP interdisk magnetostatic coupling, as interpreted in ref. 68. A vortex-type configuration is therefore corroborated by the value of the IP initial susceptibility $\chi(0)$ *versus* aspect ratio.

Let us now focus on OOP magnetization and differential susceptibility.[66,77,78] The OOP loop, displayed in Fig. 3(a), (b), exhibits a quasi-null remanent magnetization M_r, and a nearly perfect linearity around zero field. The low remanence, consistent with the vortex state, should stem from the vortex core only. The good signal-to-noise ratio of the VSM curves enables M_r to be quantified. After an accurate loop recentering around zero, M_r has been determined as $M_r = 0.0073 \times M_S$, lower than one percent of the saturation magnetization. Considering its very small amplitude, this remanent magnetization is neglected in the following model.

Modelling of the magnetic pillar properties

In this section, a phenomenological expression with a tanh function is used to fit our experimental OOP $M(H)$ data. It subsequently eases the calculation of the force expression but it does not have a particular physical justification in relation to the magnetization process:

$$\mu_0 M = \tanh(K \cdot \mu_0 H) \quad (1)$$

yielding:

$$\mathrm{d}(\mu_0 M)/\mathrm{d}(\mu_0 H) = K/\cosh^2(K \cdot \mu_0 H) \quad (2)$$

as illustrated by the red color curves in Fig. 3(a)–(c). The phenomenological constant K depends on the pillar shape, with here $K = 2.85$ for $R = 1.5$ μm. An average error of ~2% between $\mu_0 H = 0.032$ and 0.68 T has been evaluated in the OOP loop fit. The experimental OOP $\mathrm{d}M/\mathrm{d}H$ presents a near-Gaussian shape, in which however two up and down spikes are added, on back and forth branches. The coefficient K has been thus chosen as a reasonable trade-off, for taking into account the differential susceptibility in the range of field used in the optical experiments (~0.35 to 0.65 T), and its upward peak only in the zero field vicinity, as shown in Fig. 3(c).

Similarly, membrane embedding pillars of the same thickness and various diameters (2; 3; 4 μm) have been characterized and modelled. The corresponding values of K in eqn (1) were determined: 2.2; 2.85; 2.85, respectively for pillars of radii $R = 1$; 1.5; 2 μm, taking into account the NiFe upper rings presence (see Fig. 2(c–e)) for radii of 1.5 and 2 μm, only.

External magnetic field, generated on membranes

For conducting the membrane actuation, a NdFeB magnet is mounted on a micrometric positioner, enabling controlled micrometric displacements. The magnetic field, generated on the embedded magnetic pillars, has to be evaluated. The magnet consists of a parallelepiped of dimensions $2a = 5$ mm; $2b = 20$ mm; $h = 20$ mm, respectively along the OX-, OY-, and OZ-axes. As imaged in Fig. 4(a), it faces the membrane suspended in a vertical XY plane. The membrane is lit by a green laser beam. Its uniform magnetization M_{MAG}, given at $\mu_0 M_{MAG} \sim 1.29$ T, is parallel to its OZ axis. The field component B_Z along the OZ axis has been measured and modelled in the vicinity of the magnet, as a function of Z (distance magnet membrane along the OZ axis) (see Fig. 4(b)). The B_Z field component as a function of X of lesser importance for this study is presented in

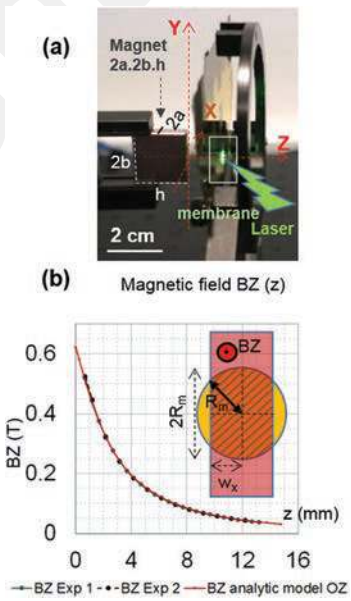

Fig. 4 Experimental and modelled magnetic field B_Z, along the OZ axis, generated by the NdFeB magnet, $\mu_0 M_{MAG} = 1.29$ T, 20 mm × 20 mm × 5 mm; 5 mm-width //0X axis; membrane in the XY vertical plane, radius $R_m = 4$ mm; OY axis vertical, XZ plan horizontal, (0, 0, 0) centered on the magnet face. Analytic model of "two charged surfaces" $B_Z(X, Y, Z) = B_Z1 - B_Z2$, according to eqn (3). (a) Photo of the magnet facing the membrane; in green color, the laser beam impacting on the membrane. (b) $B_Z = f(Z)$ in air, along the OZ axis, $(X, Y) = (0, 0)$. Experimental curves B_Z in dark colors, model in red color. See in ESI 2† the experimental and modelled X-dependence of $B_Z(X, 0, Z)$. A simplified model of B_Z is derived: in (b), a sketch showing the impact of the rectangular magnet on the membrane (yellow color), outlined by the orange-hatched reduced surface S_{red}. B_Z is assumed to be constant, $B_Z(X, Y, Z) = B_Z(0, 0, Z)$ on the hatched surface S_{red}, and $B_Z(X, Y, Z) = 0$ on the yellow color periphery. (See S_{red} expression in the text.) S_{red} ~80% of the membrane surface $S_m = \pi R_m^2$; $2 \times w_x \approx 5.5$ mm, width slightly larger than the magnet's one; S_{red} correlated to $B_Z(X, 0, Z)$ averaged along the OX axis in ESI 2.†

ESI 2.† The latter $B_Z(X)$ form is replaced by a simplified model, intended to produce on average equivalent magnetic forces on the membrane surface S_m. The small 5 mm-OX width of the magnet, which generates non-uniform $B_Z(X)$ near the membrane edges, is taken into account as presented in Fig. 4(b). Instead of varying the field in the *XY* plane, the effective surface is reduced. $B_Z(X, 0, Z)$ is supposed to be uniform and equal to $B_Z(0, 0, Z)$ on a reduced surface S_{red} and null on the remaining peripheral surface S_m–S_{red}. The reduced surface S_{red}, hatched in Fig. 4(b), is expressed as a function of the membrane radius R_m and of the magnet "impact" $2w_x$, as follows: $S_{red} = 2\cdot\left[\left(w_x\cdot\sqrt{(R_m{}^2 - w_x{}^2)}\right) + R_m{}^2\cdot\tan^{-1}\left(w_x/\sqrt{(R_m{}^2 - w_x{}^2)}\right)\right]$. The surface S_{red} thus represents 80% of the membrane surface $S_m = \pi R_m{}^2$, considering the width $2 \times w_x \approx 5.5$ mm, for the magnet (5 mm × 20 mm × 20 mm) close to the membrane without contact, and $R_m = 4$ mm.

Due to their negligible dimensions compared to the magnet size, the magnetic pillars within the membranes are considered point like. The applied field is thus quasi-uniform over their whole micrometric volume. With a reference frame centered on the external *XY* magnet face, B_Z is expressed at the coordinates $(X, 0, Z)$ by a classical electrostatic-like field model. The magnet is modelled by two surfaces of opposite charges, perpendicular to M_{MAG}, separated by the distance h, without any volumic charge density (div $M_{MAG} = 0$). Each magnetic surface bears a constant charge density $\sigma = \pm M_{MAG}$. By integration of the elementary fields generated by each unit of area, B_Z is analytically expressed at a point $(X, 0, Z)$, as follows:

$$B_Z(X, 0, Z) = [b_Z(X, 0, Z) - b_Z(X, 0, (Z + h))]$$
where
$$b_Z(X,0,Z) = \left(\frac{\mu_0 M_{MAG}}{4}\right)\cdot 2\cdot\left[\tanh^{-1}\left(\frac{(X+a)\cdot b}{Z\cdot\left(\sqrt{(X+a)^2+b^2+Z^2}\right)}\right) - \tanh^{-1}\left(\frac{(X-a)\cdot b}{Z\cdot\left(\sqrt{(X-a)^2+b^2+Z^2}\right)}\right)\right] \quad (3)$$

As illustrated in Fig. 4(b), the model fits perfectly with the field $B_Z(Z)$ measured by a Hall sensor. The fit of $B_Z(X, 0, Z)$ as a function of X, presented in ESI 2,† supports the simplified $B_Z(X)$ model described above, based on the sketch in Fig. 4(b). The gradient $dB_Z(0, 0, Z)/dZ$, required in the force calculation, is derived from the analytical expression of B_Z, yielding:

$$dB_Z(0,0,Z)/dZ = \left(\frac{\mu_0 M_{MAG}}{4}\right)\cdot 4\cdot[g(Z+h) - g(Z)]$$
where
$$g(Z) = (a\cdot b\cdot(a^2 + b^2 + 2\cdot Z^2))/\left((a^2+Z^2)\cdot(b^2+Z^2)\cdot\left(\sqrt{a^2+b^2+Z^2}\right)\right). \quad (4)$$

Magnetic forces and pressure exerted on membranes

The magnetic force exerted on the membranes is mostly unidirectional along the OZ axis. In the experimental configuration described in Fig. 4, the magnet is brought close to the membrane surface. B_Z constitutes the main active component of the field acting on the magnetic pillars. The in-plane field components (B_X, B_Y) are negligible over most of the membrane surface, except potentially near the OX transverse edges; however their sum is null by symmetry. Moreover, a residual magnetic force parallel to the *XY* plane would not yield any tangible deformation, the membrane degree of freedom being essentially out of plane. As developed below, the membrane OOP curvatures will remain small compared with their diameter (out-of-plane deformation less than 1% of their diameter). Thus, a potential planar force F_X or F_Y, projected on a normal of the concave membrane, remains negligible and thus ineffective in the OOP direction. Let us therefore consider F_Z as the only magnetic force involved in the membrane actuation. F_Z is basically expressed as $F_Z(Z) = V_P\cdot\mathrm{grad}(M\cdot B)$, where $B = \mu_0 H$ is generated by the magnet, on a pillar of magnetization M, located at the distance Z from the magnet face, V_P the magnetic pillar volume, and $-V_P M\cdot B$ the magnetic potential energy of the moment $V_P\cdot M$ in the field B. The gradient includes a contribution of the OOP differential susceptibility, being derived as:

$$F_Z(Z) = V_P\cdot\left(\frac{dM}{dB_Z}(Z)\cdot\frac{dB_Z}{dz}(Z)\cdot B_Z(Z) + M(Z)\cdot\frac{dB_Z}{dz}(Z)\right) \quad (5)$$

developed using the expressions of eqn (1)–(4), as a function of Z: (i) OOP pillar magnetization $M(Z)$ may be expressed by eqn (1) and thus (ii) OOP differential susceptibility $\mu_0\cdot d(M)/dB_Z$ by eqn (2); (iii) the magnet field B_Z is given by eqn (3), and (iv) its gradient dB_Z/dZ by eqn (4).

The analytical model of the magnetic forces $F_Z(Z)$ is illustrated in Fig. 5(a), stemming from the fit of the hysteresis loops by the TANH model and the analytical expression of B_Z. It yields the quantification of the magnetic forces on a single NiFe pillar, as a function of the magnet position. In particular, close to the magnet face ($Z \sim 0$), $F_Z \approx 1.3$ nN on a pillar of 3 μm diameter and 1.25 μm thickness, by fitting $K \sim 2.85$ in eqn (1). Furthermore, the force F_Z exerted on a NiFe pillar of larger aspect ratio, 1 μm-diameter and 4 μm-thickness requiring $K \sim 11$ in eqn (1) results in $F_Z \approx 0.4$ nN, a lower order of magnitude due to the lower magnetic volume in this particular case.

The magnetic forces $F_Z(Z)$ exerted on the array of pillars embedded in the membrane are then converted into a pressure $P_Z(Z)$ exerted on the suspended membrane. The aim is to predict the resulting membrane deformation when approaching the magnet at the distance Z. In the further mechanical model, the load is assumed to be uniformly dis-

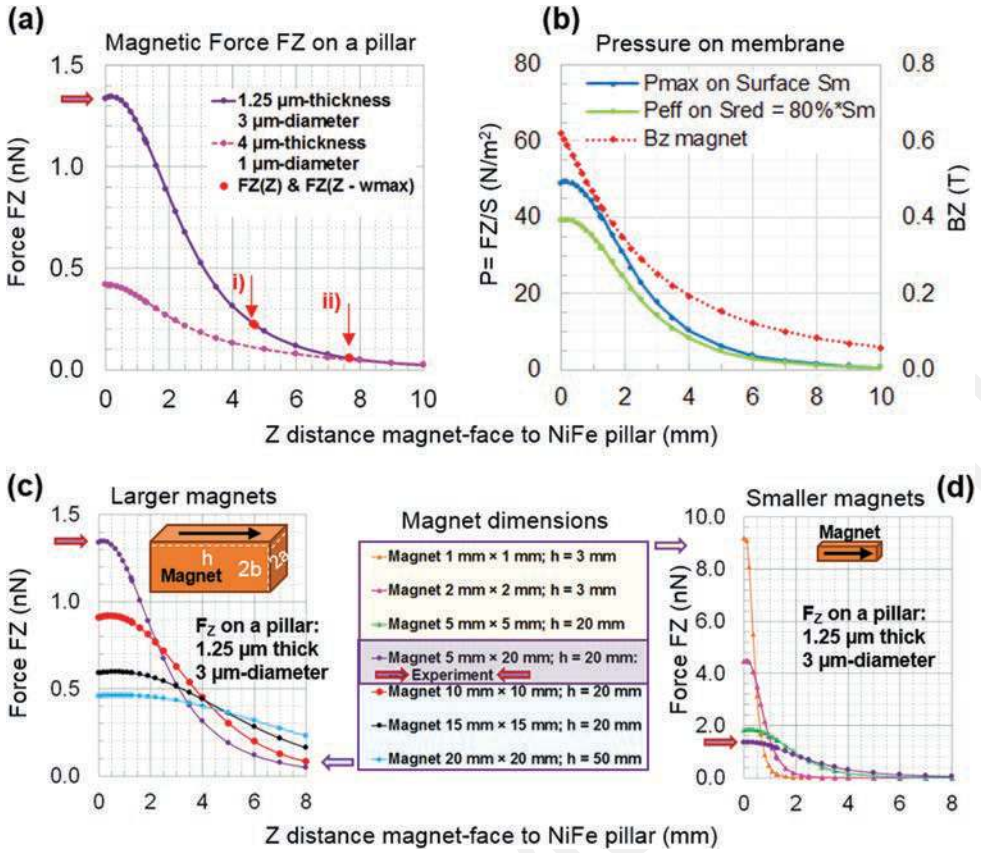

Fig. 5 Modelled magnetic forces F_Z, generated by the magnet on NiFe pillars, and resulting pressure P_Z loading the membrane tested in optics (membrane of surface S_m, diameter 8 mm, $P_Z \sim \sum(F_Z/S_m)$). Experimental NdFeB magnet of section $2a \times 2b$ = 5 mm × 20 mm, height h = 20 mm, $\mu_0 M_{MAG}$ = 1,29 T; NiFe pillars of $\mu_0 M_s$ = 1 T. (a) (1) F_Z on a NiFe pillar of ∅ 3 µm, thickness 1.25 µm, imaged in Fig. 2(e–g); $\mu_0 H_{SAT} \approx 0.36$ T, saturated for $Z \leq 1.7$ mm. (2) F_Z on a NiFe pillar of ∅ 1 µm, thickness 4 µm, imaged in Fig. 2(a), $\mu_0 H_{SAT} \approx 0.12$ T, saturated for $Z \leq 6$ mm. In (i) and (ii) respectively coincide 3 close dots: (i) (1) $F_Z(Z = 4.7\text{ mm}) = 0.220$ nN; (2) $F_Z(Z = 4.7\text{ mm} - 38\ \mu\text{m}) = 0.224$ nN yielding F_Z variation of 1.8% for $dZ = w_{max} = 38$ µm; (3) similarly for $dZ = 50$ µm, $F_Z(Z = 4.7\text{ mm} - 50\ \mu\text{m}) = 0.225$ nN. (ii) (1) $F_Z(Z = 7.7\text{ mm}) = 0.0558$ nN; (2) $F_Z(Z = 7.7\text{ mm} - 23.8\ \mu\text{m}) = 0.0564$ nN yielding F_Z variation of 1% for $dZ = w_{max} = 23.8$ µm; (3) similarly for $dZ = 50$ µm, $F_Z(Z = 7.7\text{ mm} - 50\ \mu\text{m}) = 0.0570$ nN. (b) Pressure $P_Z(Z)$ on a membrane shown in Fig. 2(c), NiFe thickness = 1.25 µm; hexagonal array; unit cell of surface S_{cell} with pillars of radii: 1 × (R = 2 µm) + 3 × (R = 1 µm); $P_Z(Z) = \sum(F_Z)/S_m = [1 \times F_Z(R = 2\ \mu\text{m}) + 3 \times F_Z(R = 1\ \mu\text{m})]/S_{cell}$. In blue color: a maximized $P_{Zmax}(Z)$, with $B(X, Y, Z)$ assumed = $B(0, 0, Z)$ over the whole surface S_m; in green color: an effective pressure P_{Zeff}, with $B(X, Y, Z)$ assumed = $B(0, 0, Z)$ over a reduced surface S_{red}, and B = 0 near membrane edges; $S_{red} \approx 80\% \times S_m$. $P_{Zeff} = 0.80 \times P_{Zmax}$. In red color: $B_Z(Z)$ inducing the pressure. (c–d) Modelled forces F_Z, exerted by magnets of various dimensions on a NiFe pillar of ∅ 3 µm, thickness 1.25 µm, along the OZ axis only; F_Z compared to F_Z from our experimental magnet of section 5 mm × 20 mm, height h = 20 mm. (c) Magnets of larger sections than the membrane surface S_m, two heights, yielding smaller forces on OZ near Z = 0: appropriate if the magnet is placed relatively "far" from the membrane. (d) Magnets of smaller sections than the membrane surface S_m, two heights, yielding locally larger forces on OZ near Z = 0, appropriate if the magnet is placed close to the membrane (requiring thus more flexibility).

tributed over the membrane area, disk of radius R_m = 4 mm, and surface $S_m = \pi R_m^2$, imaged in Fig. 1(c). A large centered portion of the membrane surface is effectively subjected to a mostly uniform magnetic field. As detailed above, the potential variation of $B_Z(X, Y, Z)$ in the plane XY along OX is taken into account by considering the magnetic field $B_Z(X, 0, Z) = B_Z(0, 0, Z)$ uniform on S_{red}, and null outside (Fig. 4(b)). Hence, the average pressure $P_{Zeff}(Z)$ exerted on the whole surface S_m is expressed as follows: for a number N_{red} of identical pillars embedded in the reduced surface S_{red}, $P_{Zeff}(Z) = [N_{red} \times F_Z(Z)]/S_m$. A maximal pressure is furthermore defined by the expression $P_{Zmax}(Z) = [N_{max} \times F_Z(Z)]/S_m$, reflecting the case of a field $B_Z(0, 0, Z)$ being uniformly applied on the whole membrane S_m, embedding N_{max} number of pillars. The ratio $P_{Zeff}(Z)/P_{Zmax}(Z)$ equals S_{red}/S_m calculated above at around 80% for the relative dimensions of our magnet and membrane. Both pressure curves are shown in Fig. 5(c), with $P_{Zeff}(Z) = 0.80 \times P_{Zmax}(Z)$, concerning the membranes used below.

Magnetic forces F_Z exerted on a pillar depend on the applied magnetic field and its gradient, *i.e.* on the magnetic source design. Various magnet compositions, shapes and dimensions can be chosen, depending on the size of the membrane, its distance Z to the magnet, and its flexibility. A few magnet geometries were compared with the one used here, the forces F_Z on a pillar being calculated in Fig. 5(c–d). On the one hand, smaller magnets such as small magnetic tips, which locally create larger gradients, produce larger forces. However, the field is applied more locally, requiring very elastic PDMS

and close approach of the field source. On the other hand, magnets with sections covering the full membrane surface S_m (*e.g.* magnet section of 10 mm × 10 mm, instead of the 5 mm × 20 mm used here) create smaller forces close to the magnet face (at small Z), and larger forces at longer distance. The geometry of the present magnet is then considered as a good compromise for generating sufficient forces between Z = 3 to 8 mm yielding large membrane deformations from Z = 0 to 2 mm.

For a further utilization of the magneto-elastic membrane in adaptive optics, arrays of local actuators could be used, instead of the global one presented here. As presented in ref. 57, arrays of planar microcoils, or more efficiently, small magnet/electromagnet arrays could be designed, formed of magnetic tips acting very locally on membrane portions, displaced along the OZ axis, for instance, by current coils.[57] For instance, the calculation of forces F_Z generated by a magnetic NdFeB tip of section 10 μm × 10 μm and height h = 100 μm yields: F_Z = 160 nN at $Z \approx 7$ μm, and 460 nN at $Z \approx 4$ μm, which are respectively 100 and 320 times larger than with our experimental macroscopic magnet, however at a very local range of less than a few tens of micrometers. Forces from tips of millimetric dimensions can be likewise compared (Fig. 5(d)).

Remember that the force F_Z depends on B, its gradient, but also on the susceptibility dM/dB of the magnetic pillar material.

From this point, we will focus exclusively on the magnet described in Fig. 4, and membranes investigated in optical experiments, developed in the last section. Such membranes tested in optics are similar to the one imaged in Fig. 2(c), embedding hexagonal arrays of NiFe pillars of two different radii, R_1 = 1 μm and R_2 = 2 μm. In the pillars' distribution appears the unit cell of surface S_{cell} = 10 μm × [10 × (√3/2)] μm = 8.66×10^{-11} m^2, with a proportion of one R_2 for three R_1 pillars. The total force F_{Zcell} exerted on the unit cell is obtained by summing the elementary forces calculated on each pillar, such as: $F_{Zcell} = 1 \times F_Z(R = 4\ \mu m) + 3 \times F_Z(R = 2\ \mu m)$, the two hysteresis loops being modelled using K = 2.2; 2.85 in eqn (1), respectively, for R_1 and R_2, (thicknesses of 1.25 μm). The maximal and effective pressures loading the membrane have been quantified (see Fig. 5(b)), yielding $P_Z \sim 50$ N m^{-2} and $P_{eff} \sim 40$ N m^{-2} when such a membrane is close to the magnet (near Z = 0). For each magnet position Z, the graph in Fig. 5(b) shows simultaneously the magnetic field generated on the membrane (red color curve) replicated from Fig. 4, and the induced loading pressure. The resulting membrane deformation is then modelled in the next section.

Modelling membrane deformation *vs.* magnetic forces

The membrane becomes concave, attracted by the magnet, when submitted to the constant or slowly varying magnetic field $B_Z(Z)$. The membrane profile $w(r)$ along OZ, in particular the maximum deflection $w_{max} = w(0)$, has been calculated analytically using the "clamped circular plate" model from the "theory of plates" (Timoshenko and Woinowsky-Krieger, 1959)[79] and (Zhang, 2016).[80] Our membranes essentially consist of PDMS/gold bilayers. When no external forces are exerted, they are flat. Since the embedded magnetic material is not continuous and represents only a small fraction of the total area (at most 25%), its contribution to membrane elasticity has not been considered in the present calculation. The mechanical properties of PDMS and Au layers have been therefore expressed and compared: (1) gold: Young's modulus E = 80 GPa; Poisson's ratio ν = 0.42; thickness h_{AU} = 100 nm; (2) PDMS: E = 1.5 MPa; ν = 0.49; h_{PDMS} = 5 μm (membrane radius R_m = 4 mm). Due to the very large difference in Young's modulus between Au and PDMS (more than 4 orders of magnitude), the rigidity of the membrane is determined by the Au layer despite its lower thickness. The membranes have therefore been considered as elastic plates made of gold (Au) only in the mechanical model. From the experimental point of view, the presence of the PDMS layer remains however important for the magnetic pillar fabrication process. Zhang's model is then applied, assuming no initial in-plane tension, the assumption confirmed in hindsight through the diffraction signal measured in zero field on the suspended membranes, directly related to the "as grown" pillar periodicity (see Optical section). The membrane profile $w(r)$, $r(0 \le r \le R_m)$ being the distance from the membrane center, is expressed as:[80]

$$w(r) = w_{max} \cdot \left(1 - \frac{r^2}{{R_m}^2}\right)^i \qquad (6)$$

with i = 2, $w_{max} + (0.4118 + 0.25\ \nu - 0.16088\ \nu^2)({w_{max}}^3/h^2) = (P_z(Z) \cdot {R_m}^4)/(64D)$ and the membrane bending stiffness $D = (E \times h^3)/(12 \times (1 - \nu^2))$. Zhang's model uses either i = 2 or 1, according to whether the clamped condition of the zero slope is required or not.[80] Our experimental situation corresponds to the former case (i = 2) since the membrane edge is plated on the silicon substrate. The membrane profile is represented in Fig. 6(a), on which is outlined in green color an arbitrary section where the incident laser beam hits the membrane. Since the laser diameter D_λ = 3.5 mm is smaller than the membrane radius, the incident beam may be directed towards various areas of the membrane, and thus may illuminate different portions of this membrane profile. It should be noted that the optical model developed below enables to select, as one of its inputs, which portion of the membrane profile is illuminated. The maximal deflection w_{max} has been calculated, and plotted in Fig. 6(b) *versus* the exerted pressure P_Z. As benchmarks, two deflection values w_{max}, determined from the optical experiments, are indicated by blue straight lines in Fig. 6(b).

The magneto-mechanical model led to the deflections w_{max} triggered by the application of magnetic fields. It should be mentioned that the forces $F_Z(Z)$ exerted on the magnetic pillars were supposed to be independent of the membrane deformation: $F_Z(Z) \sim F_Z(Z - w_{max})$. Indeed, the resulting deflections w_{max} (a few tens of micrometers) are negligible compared to the magnet-to-membrane distance Z (~1 to 10 mm). More precisely, $F_Z(Z - w_{max})$ is applied at

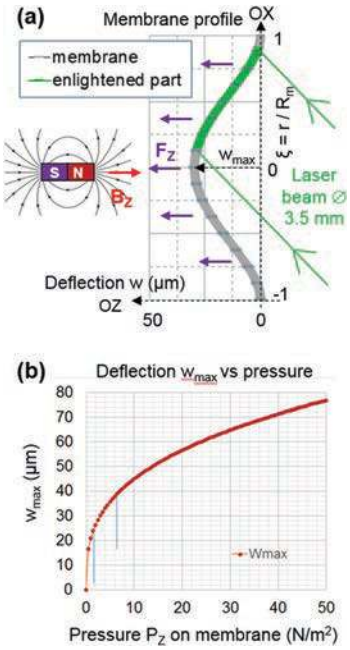

Fig. 6 Profile and deflection of the membrane, modelled as a clamped circular plate, of radius R_m = 4 mm; thickness h_{PDMS} = 5 μm; h_{AU} = 100 nm. Model considering the Au layer only; with E = 80 GPa; ν = 0.49. (a) Membrane cross section profile $w(r)$ in grey (+green) colors, using i = 2 in eqn (6); r distance to center. In green color is shown an arbitrary location of the incident laser beam on the membrane; the laser beam of diameter D_λ = 3.5 mm, smaller than the membrane radius R_m = 4 mm. (b) Deflection $w_{max} = w(0)$, *versus* the load pressure $P_Z(Z)$.[80] The blue color lines indicate two particular deflections determined from the experiment + model: w_{max} = 23.8 μm from P_Z = 1.5 N m^{-2} and w_{max} = 38 μm from P_Z = 6 N m^{-2} corresponding to situations where the magnet was placed respectively at $Z \sim 7.7$ mm and 4.7 mm, *i.e.* $B_Z \sim 0.09$ T and 0.16 T (P_Z and B_Z illustrated in Fig. 5(b)).

the membrane center, while $F_Z(Z)$ at the membrane edges. Their slight difference $F_Z(Z) - F_Z(Z - w_{max})$ was *a posteriori* evaluated by our magneto-mechanical model, as shown in Fig. 5(a) on the NiFe pillars of ∅ 3 μm, 1.25 μm-thick. Each red dot labelled (i) and (ii) on the curve $F_Z(Z)$ comprises 3 forces nearly coinciding, modelled with and without membrane deflections. In particular, magnets placed at (i) Z = 4.7 mm yielding w_{max} = 38 μm, at (ii) Z = 7.7 mm, yielding w_{max} = 23.8 μm, produce F_Z edge-to-center variations of, respectively, 1.8% and 1% (see Fig. 5(a) caption). Self-consistently calculating the pressure P_Z and the deformation w_{max} would result in a correction of less than 1.8% or 1%. Forces $F_Z(Z)$ can therefore be reasonably considered as quasi-identical on a flat or deformed membrane, given our experimental data.

Optical characterization of the magneto-elastic membrane deformation and modelling

The next objective was to characterize the membrane optical response to magnetic field-induced actuation. The vertical membrane was illuminated by a horizontal green laser beam (wavelength λ = 532 nm), and submitted to the magnetic field generated by the NdFeB magnet. Both reflected and transmitted beam variations were studied as a function of magnet-membrane distance. The membranes were first optically characterized in their rest configuration *i.e.* in zero external magnetic field. The NdFeB magnet was subsequently approached thanks to a micrometric stage and the resulting optical response of the concave membranes was measured.

Diffraction of the laser beam by the membranes

First of all, the observation of a transmitted beam indicates that the PDMS membranes are semi-transparent, despite the presence of the embedded pillars and of the 100 nm-thick Au layer. The reflected and transmitted images consist of interference and diffraction patterns. As a matter of fact, such optical patterns can be expected from these membranes since the spacing between pillars and their size are of the order of the laser wavelength. As shown in Fig. 7(a), the optical diffraction patterns were recorded on a screen without inserting the lens on the optical paths. Pattern evolution is shown for instance in Fig. 7(b–c), as a function of the magnet position. The OX and OY axes are represented in Fig. 7(b–c). We mention that the reflected patterns were captured either from the front or from the back side of the semi-transparent screen used in the reflection. The reflected image is viewed on its front side in Fig. 7(a–b) and on its back side in Fig. 7(c).

In zero magnetic field, the grating being flat, both reflection and transmission diffraction patterns consist of arrays of light spots, periodically spaced along the OX and OY axes on the screen. Surprisingly, the membrane embedding the hexagonal array produces a rectangular diffraction pattern, illustrated in Fig. 7. Its hexagonal periodicity does not produce any clear influence. As mentioned in the first section, the prominent rectangular cells made by the dark upper rings shown in Fig. 2(c) form the visible rectangular grating, optically and visually predominant. This is due to the dominant optical contrast produced by the particles in rectangular arrangement as compared to the one produced by the particles in hexagonal arrangement.[81] The resulting 2D rectangular grating is oriented in the vertical *XY* membrane plane, with 8.66 μm and 10 μm pitches respectively parallel to the OX axis and OY axis.

A first observation is that the incident angle θ_0 has a different impact on the diffraction patterns along OX- and OY-axis. The aspect ratio of the rectangular 2D diffraction pattern (*i.e.* periodicity along OX divided by periodicity along OY) increases with θ_0: increasing θ_0 enlarges the diffraction spot spacing l_x along the horizontal OX axis, without modifying the spot spacing l_y along the vertical OY axis. This results from the fact that since the laser beam is within the plane defined by OX and the normal to the membrane, the difference of optical paths between successive pillars aligned along the y direction is independent of θ_0 and only depends of the OY pillar spacing in the membrane. On the contrary, the spot spacing l_x along the horizontal OX axis depends on θ_0, as modelled here below.

We have first checked the correlation between the pitches of the grating d_y and of the diffraction patterns l_y along the vertical OY axis: $d_y \approx (\lambda \cdot D)/l_y$ where D is the distance membrane to screen. The two membranes imaged in Fig. 2(c–d) were charac-

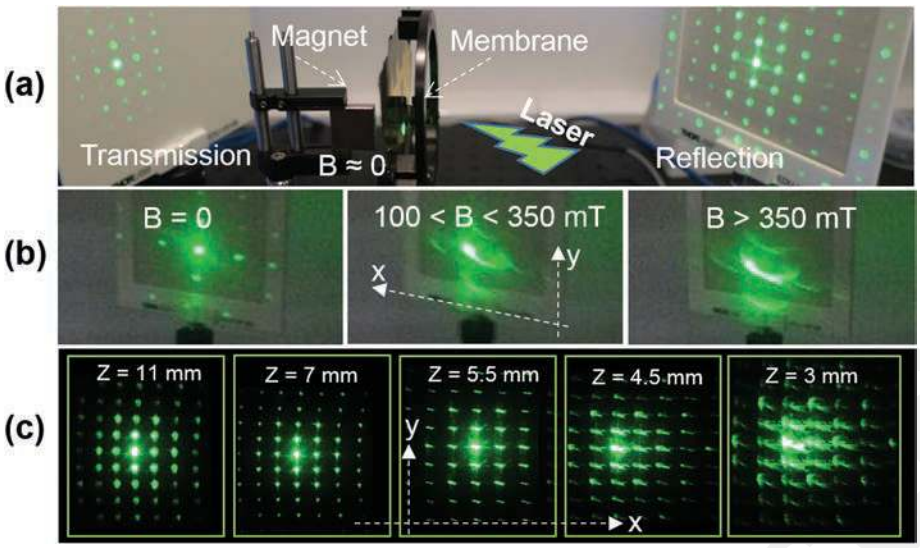

Fig. 7 Photos of diffraction patterns in reflection and transmission, from an incident laser beam on the targeted membrane. Rectangular grating of pitches 8.66 μm × 10 μm. (a) Optical set-up; membrane in a quasi-null magnetic field. (b) View of the front side of the semi-transparent screen: effect of an increasing magnetic field *B*, in reflection. (c) View of the semi-transparent screen back side: diffraction patterns in reflection, *versus* the magnet distance *Z* (mm). Observation, at *Z* = 7 mm: the deformation of the membrane yielded the focus of the laser bean on the screen (b–c) (OX, OY) axis directions, traced on front/back sides of the semi-transparent screen used in reflection.

terized. Their respective *Y* pitches from the lithography masks should be 10 and 3 μm, which have been corroborated by direct microscopy imaging (Fig. 2). The *Y*-pitch measured at the center of the diffraction patterns is respectively l_y = 2.1 and 6.8 cm, yielding the calculated d_Y = 10.13 and 3.12 μm, in good agreement with the actual *Y*-pitches in the membrane.

Diffraction pattern evolution from the concave membrane in the external magnetic field

The membrane becomes concave by application of the external magnetic field. The resulting diffraction patterns and their progressive evolution during the membrane actuation, from planar to concave, have been observed and modelled, in particular in reflection.

We have first compared the reflection and transmission experimental patterns. At zero magnetic field, the membrane is planar. Both beams produce similar types of diffraction patterns, forming rectangular spot matrices for any θ_0, as illustrated in Fig. 7(a). However, reflected and transmitted beams interact differently with the membrane, resulting in very different transmitted and reflected diffraction patterns when the membrane becomes concave under magnetic field, as shown in Fig. 8(a). Clearly, the reflected pattern is highly deformed, whereas the transmitted one remains unchanged. This immediate observation is coherent with basic optical principles, as outlined in the ref. 82. Indeed, let us consider the 0^{th} order of diffraction, the brightest spot at the center of the diffraction pattern. Its position in reflection, on the horizontal OX axis on the screen, is determined by the specular reflection. Notably, the incidence and reflection angles θ_0 depend on the normal-to-the-membrane direction, which precisely varies over the whole membrane surface when the membrane is concave. All the reflected rays are directed at $2 \times \theta_0$ from the incidence direction, highly variable angle *versus* the impact point of each ray on the concave membrane surface. The sum of these out-of-phase waves can produce a quite extended diffraction/interference pattern along the OX axis. The experiment shows that the interference spots are progressively converted into sets of fringes with possible shadow areas, when the field is increased. An extension of the spot along the vertical OY axis may occur, since the membrane is clamped on its whole periphery, and its deformation is thus not only cylindrical. However the spot deformations are less marked along OY than along OX, since the laser beam is horizontal – *i.e.* the incidence angles present less variation along the vertical membrane profiles than along the horizontal profiles. By contrast, the 0^{th} order of diffraction in the transmitted pattern remains fixed by the direction of the incident beam, invariant with the normal-to-the-membrane direction. It thus remains independent of the concavity. A non-planar membrane will influence the transmitted beam by only negligible and invisible variations of the optical paths, since our current membrane deflections w_{max} remain here negligible as compared to the membrane diameter. Both reflection and transmission patterns shown in Fig. 8(a) have been recorded with the same applied magnetic field *B* and the same incident angle θ_0. Moreover, reflection patterns turn out to be highly sensitive to small micrometric/even nanometric membrane deflections. The following optical model aims at fitting the shape of the diffraction patterns of a concave membrane along the horizontal direction of the screen.

A schematic cross section of the concave membrane is presented in Fig. 8(b), on the horizontal *XZ* plane, OZ being perpendicular to the initial plane *XY* (in zero field). The membrane profile may be modelled in particular by the "clamped

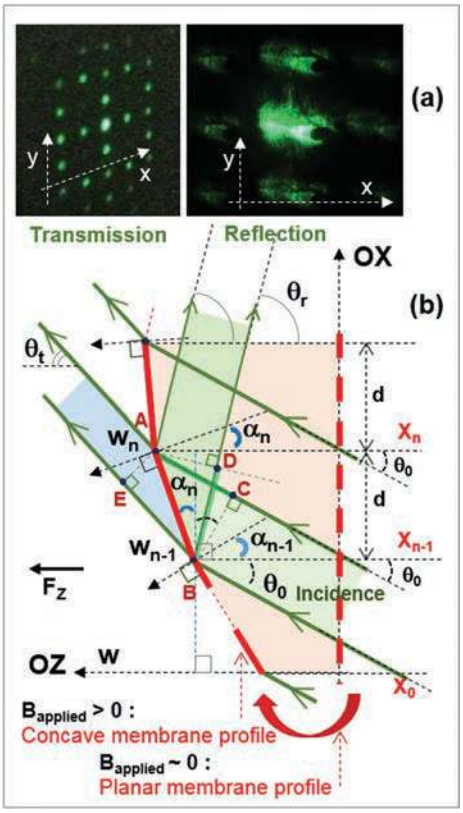

Fig. 8 Optical experiment and scheme: reflected, transmitted and incident beams. (a) Photos of the diffracted patterns in transmission and reflection, for a given B_Z and θ_0 (b) Scheme of the light beams (green & blue colors) on a concave membrane. Cross section of the deformed membrane, either planar (red color dashed line), or concave (red solid lines). Lengths and angles used in the model: θ_0 incident angle, w_n deflection of the pillar n, on the OZ axis. Concavity modelled as straight segments tangent to the membrane shape, linking the neighboring pillars n and $(n-1)$; d = pitch of the planar grating along the OX axis.

plate model" discussed above, usable for a circular plate. We will consider, from here, a unidimensional curved grating embedded in this membrane section, lying in the horizontal XZ plane. The resulting diffraction and interference peak intensity, and their evolution as a function of the membrane deflection, have been modelled along the OX axis. They are compared to experimental intensity curves recorded along the OX axis on the screen. The mechanical model expresses above the continuous deflection $w(r)$ for any r, the distance to the membrane center on OX, as previously described in Fig. 6. However, the large density of magnetic pillars along the membrane profile, with their pitch $d \ll R_m$ membrane radius, plus the small order of magnitude of w_{max}, enables simplifications. Our geometric model of concave grating has been built with the two following simplifying assumptions: (1) the concave grating profile is represented by a succession of straight segments linking each magnetic pillar to both their neighboring pillars; and (2) each pillar (labelled by their respective number "n", located at $X_n = n \times d$ on the OX axis) is supposed to be physically displaced by a simple horizontal projection along OZ when the membrane is deformed. They are thus located on the concave profile line at the distance w_n from their initial position on OX. Each straight segment direction will locally define the direction of the reflected light in the optical model. They determine the normal-to-the-membrane directions, locally variable. The membrane deflection w_n at the pillar "n" is modelled by eqn (6) with $i = 2$ and $r = X_n - R_m$, leading to:

$$w_n = w(X_n - R_m) = w_{max} \cdot \left[1 - \left(\frac{(X_n - R_m)^2}{{R_m}^2}\right)\right]^2.$$

The total number of magnetic pillars N_{TOT} enclosed in the membrane along the OX diameter, is expressed *versus* the pitch of the permalloy array along OX: $N_{TOT} = (2 \times R_m)/d$. The pitch $d = 8.66$ μm and the radius $R_m = 4$ mm yield $N_{TOT} \approx 923$ pillars along the membrane diameter. However, the laser beam hits only a portion of the membrane surface, since the beam diameter $D_\lambda < R_m$, as sketched in Fig. 6(a) by the green color line, highlighting the laser position on the membrane profile. Hence, $N = (D_\lambda/d) \times (1/\cos\theta_0)$ is the number of magnetic pillars impacted by the laser beam in the planar membrane profile, smaller than half N_{TOT} for small incident angles. For selecting the position of the laser beam on the membrane profile, a number n_{min} is required, labelling the first of the lit pillar series along the OX axis (with $n_{min} + N - 1 \leq N_{TOT}$). $D_\lambda = 3.5$ mm and $d_X = 8.66$ μm yield $N \approx 3500/8.66 \approx 404$ illuminated pillars at normal incidence. We have tested various numbers of pillars impacted by the laser, such as $300 < N < 450$ in the optical model, considering a reduced N for a laser beam not perfectly centered on the membrane.

Reflected light intensity was modelled, based on the concave grating schematized in Fig. 8(b). A local angle α_n was defined on each pillar: $\tan\alpha_n = (w_n - w_{n-1})/d$, for intermediate calculations. The geometrical construction leads to the optical path difference between two adjacent light rays, reflected on the pillars $n-1$ and n, while taking into account the local concavity of the membrane, as follows:

$$\begin{aligned}(BD - CA)_n = &[d\cdot(\sin\theta - \sin\theta_0)] \\ &- [(w_n - w_{n-1})\cdot(\cos\theta + \cos\theta_0)]\end{aligned} \quad (7)$$

where θ defines the direction of the considered reflected beam: the angle between (1) the straight line linking the membrane to the screen at the abscissa $x = x(\theta)$, and (2) the OZ axis normal to the initial planar membrane. In particular, $\theta = \theta_0$ corresponds to the 0^{th} order of diffraction in the reflection for the planar membrane only. Then, from the successive phase differences of eqn (7), using the wavenumber $k = 2\pi/\lambda$, the light distribution $U(\theta)$ reflected on N pillars, in the direction given by the angle θ, is summed up as: $U(\theta) = U^{(0)}(\theta)\cdot\left[1 + \sum_{n=1+n_{min}}^{n_{min}+(N-1)} e^{-ik\cdot(BD-CA)_n}\right]$, finally yielding the following expression:

$$U(\theta) = U^{(0)}(\theta)\cdot\sum_{n=n_{min}}^{n_{min}+(N-1)} e^{-ik[n\cdot d\cdot(\sin\theta - \sin\theta_0) - w_n\cdot(\cos\theta+\cos\theta_0)]} \quad (8)$$

leading to the light intensity $I(\theta) = \left[U(\theta)\cdot\overline{U(\theta)}\right]$.

$I(\theta)$ is modulated by $I^{(0)}(\theta) = (U^{(0)}(\theta))^2$, reflecting the Fraunhofer diffraction on the pillars of radius R, modelled as small lines of width $2R$ on the membrane profile: $I^{(0)}(\theta) = (\mathrm{sinc}(k{\cdot}2R{\cdot}p/2))^2$ with $p = \sin\theta - \sin\theta_0$, "sinc" being the "cardinal sine function".[83] We consider $\theta = a\tan(x/D)$ to derive the light intensity *versus* x along the OX axis on the screen.

Let us point out that various possible shapes of concave membranes could be inserted in eqn (8) instead of eqn (6) with $i = 2$, through various expressions of w_n. A circle-segment shape ($i = 1$ in eqn (6)), and a two-broken-lines (pointy hat) shape have been likewise coded. The latter enables a fully analytical expression of $U(\theta)$, resulting in the transformation of each spot of the planar membrane into two spots only. However, the best final fit to our experimental data was obtained with eqn (6) and $i = 2$. It is therefore the only one presented in this paper. The model, analytical till eqn (8), has required a numerical evaluation for the $N - 1$ values to be summed, N in the range of 300 to 450 pillars.

Fitting interference/diffraction patterns from planar *versus* concave membranes

The optical model is firstly applied to the membrane in its basic planar state ($w_n = 0$). As expected along OX on the screen, the light intensity profile results in a semi-periodic series of interference peaks modulated by the diffraction amplitude, yielded by eqn (8) with $w_n = 0$, as shown in Fig. 9(a). Each peak corresponds to an m^{th} order, localized at $p \equiv \sin\theta_{(m)} - \sin\theta_0 = m \times \lambda/d$, *i.e.* at the abscissa $x(m)$ on the screen, such as $x(m) = D{\cdot}\tan(\sin^{-1}(\sin\theta_0 + m{\cdot}(\lambda/d)))$, from the classical theory of the diffraction gratings.[83] The spacing $x(m) - x(m-1)$ between neighboring peaks tends to vary due to the tangent relationship between x and the diffraction angle θ. The involved semi-period either simply increases in the OX axis direction for an off-centered screen, or increases towards both sides of the intersection of the membrane normal and the screen ($\theta = -\theta_0$), if relevant. In particular, it increases symmetrically around the 0^{th} order along the OY axis, as well as along OX axis at normal incidence. This classical well-defined set of interferences/diffraction fringes from the planar membrane is the starting point for quantifying the optical response from the concave membrane (spot shift and broadening), deformed by the application of a magnetic field.

The aim is now to compare the experimentally recorded diffraction patterns highly influenced by the membrane concavity, and the model given by eqn (8). The experiments have shown large broadening of the interference spots along the OX axis in reflection, induced by approaching the magnet. The magnetic-field-independent inputs in our optical model consist of: the laser wavelength λ; the membrane radius R_{m}; the grating pitch d and pillar radius R; the membrane-to-screen distance D; the incidence angle θ_0, measured and slightly adjusted; the number of illuminated pillars N (300 to 450); and the number $n_{\min}$ localizing the laser impact. Differently, the membrane deflection parameter $w_{\max}$ results from the application of the magnetic field, and is modelled by our magneto-mechanical approach. Arbitrary values of $w_{\max}$ were firstly tested. As expected, increasing $w_{\max}$ increases the broadening of the simulated spots, potentially transformed into fringes of lower intensities along OX. An input $w_{\max} \geq 200$ μm can produce quasi-joined fringes from one spot to its neighbor, while keeping their semi-periodicity apparent; $w_{\max} \geq 700$ μm produces quasi-continuous fringes along OX. Such qualitative results match with the experiment.

The quantitative analysis is conducted in reflection, in particular for the two following experimental diffraction patterns, from the above hexagonal-array membrane. The experiments "1" and "2" display respectively 6 and 3 interference peaks remaining close to their initial position, with relatively small broadenings, as shown in Fig. 9(b), (c) and zoomed in Fig. 10(a), (b). The vertical laser spot is supposed to be vertically centered (along the OY axis) on the membrane, and potentially off-centered in the XZ plane with respect to the membrane center. The laser spot intersects the membrane profile shown in Fig. 6(a) and 7(b) in an off-centered concave line, which begins at the pillar number $n_{\min}$, first pillar of the unidimensional concave diffraction grating, and ends at pillar number $n_{\min} + N - 1$. The inputs for modelling the experiments "1" and "2", respectively, consist of: (i) the incidence angles θ_0, numbers N and $n_{\min}$, given in the Fig. 9(b)–(c) caption, slightly adjusted around the experimental and estimated values; (ii) the magnetic field applied at $Z = 7.7$ and 4.7 mm; and (iii) the resulting membrane deflection, through our magneto-mechanical model, $w_{\max} = 23.8$ μm from $B_Z = 0.09$ T and $P_Z = 1.5$ N m^{-2}, and $w_{\max} = 38$ μm from $B_Z = 0.16$ T and $P_Z = 6$ N m^{-2}. Inserting $w_{\max}$ in eqn (8) leads to the modelled diffraction patterns shown in Fig. 9(b)–(c). Adjusting N and $n_{\min}$ around their estimated values allows our magneto-mechanical-optical model (green color curves) to fit the experimental optical data (black color curves) in a reasonably good agreement. The order of magnitude of $n_{\min}$ is in good agreement with the shift direction of the interference peaks from the planar to the concave membrane, reflecting the laser spot location on the concave membrane: $n_{\min} = 530$ (Fig. 9(b) for a laser illuminating the second half of the membrane area, as sketched in Fig. 6(a) and $n_{\min} = 37$ (Fig. 9(c)) reflecting a spot enlightening the first half of the membrane. From this approach, the semi-period, the peaks shift and broadenings in the diffraction patterns from planar to concave membranes can therefore be quantified as a function of the applied magnetic field. The curves zoomed in Fig. 10(a–b) further detail the fit with the experimental envelope of single peak profiles, for both experiments "1" and "2".

The complete magneto-mechanical-optical model confirms that the magneto-elastic membranes presented here can generate large optical responses, easily detectable, for tiny concavities produced by the applied magnetic field and quantified. (Membrane deflections are in the range of only a few tens of micrometers <1% of the membrane diameter of 8 mm.) For estimating the limits of detection of the membrane deflection through the optical experiment, without improving the present experimental conditions, the optical model was used with a similar parameter set, varying only $w_{\max}$ from 0 to 10 μm. The

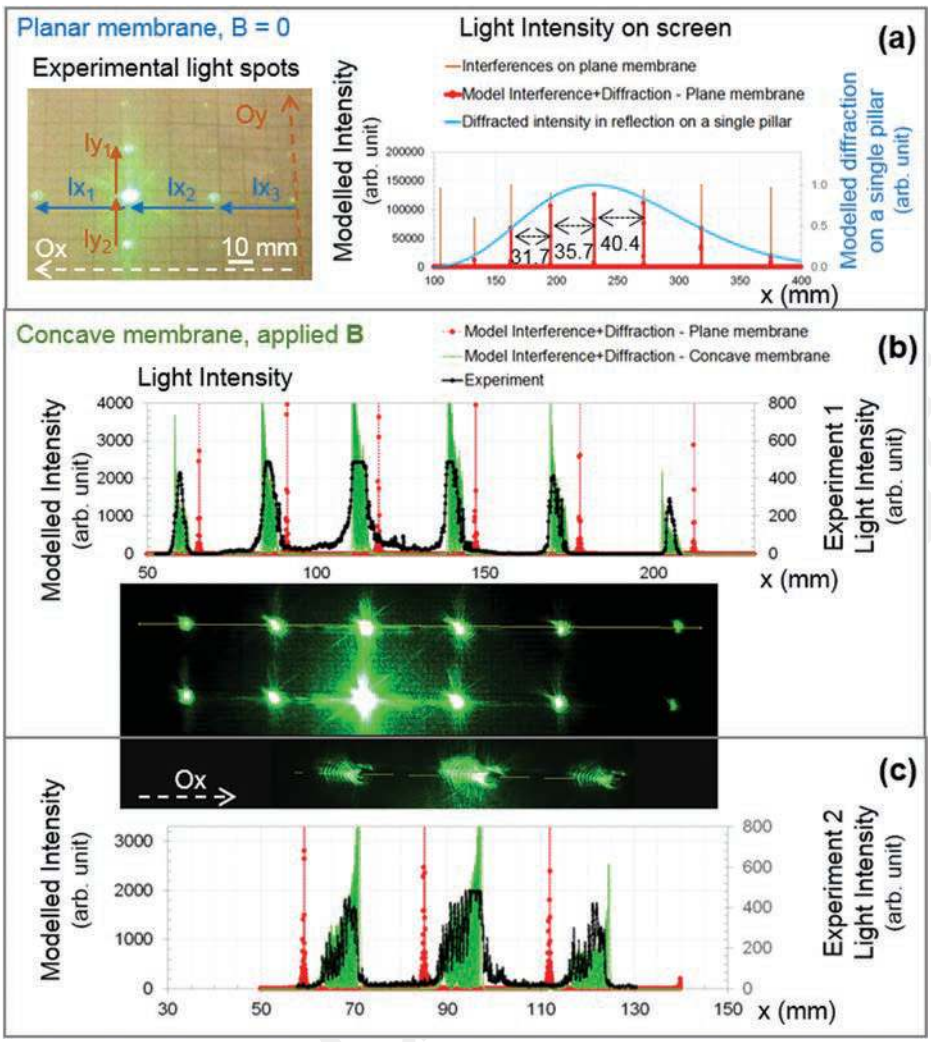

Fig. 9 Optics. Interference/diffraction patterns from a concave *versus* planar membrane, in reflection; planar membrane in $B = 0$, deformed by the applied magnetic field B. Experimental and modelled light intensity along the OX axis. Laser wavelength $\lambda = 532$ nm; membrane embedding the hexagonal array of $R = 1$ and 2 μm-radii-magnetic pillars; optical pattern yielded by the rectangular sub-array of the $R = 2$ μm-pillars, grating of 0X-pitch $d = 8.66$ μm; membrane-to-screen distance $D = 40$ cm; screen parallel to the membrane initial plane. (a) Planar membrane, in $B = 0$; $\theta_0 = 0.45$ rad; experiment spots of semi-periods $x(m) - x(m-1)$: $lx1$–39; $lx2$–35; $lx3$–32; $ly1 \approx ly2$–21 (mm), and modelled intensity, on the screen front side. (b–c) Concave membrane, in the applied B; light intensity profile parallel to the OX axis on the back side of the screen: experiment in black color, model in green color; in red color: from the planar membrane (in $B = 0$). (b) Experiment 1: 6 light spots; the magnet positioned at $Z = 7.7$ mm; optical model fitting by (i) the membrane deflection $w_{max} = 23.8$ μm, resulting from [$B_Z = 0.09$ T, $P_Z = 1.5$ N m^{-2}]; (ii) the number of pillars illuminated by the laser beam $N = 350$; (iii) the first illuminated pillar in the membrane profile $n_{min} = 530$; (iv) the adjusted incidence angle $\theta_0 = 0.288$ rad. (c) Experiment 2: 3 light spots; the magnet at $Z = 4.7$ mm; fitting parameters: (i) $w_{max} = 38$ μm, from [$B_Z \approx 0.16$ T, $P_Z = 6$ N m^{-2}]; (ii) $N = 380$; (iii) $n_{min} = 37$; and (iv) $\theta_0 = 0.209$ rad. All the light intensity profiles are modelled with 5000 points in the interval [x_{min}, x_{max}] along the OX axis on the screen.

resulting evolution of the interference fringes, displayed in Fig. 10(c) for a 0th order peak, indicates that a deflection of 500 nm could be likewise detected.

In summary, the magnetic properties of the experimental membrane were fitted by a magnetic model (eqn (1)–(2)). The stray field from the magnet used for the membrane actuation was also fitted by a theoretical model (eqn (3)–(4)). The merging of both models led the calculation of the magnetic forces (eqn (5)) and pressure exerted on the membrane. These forces were not directly experimentally measured. The modelled pressure constituted the input of the elastic plate model (eqn (6)), which was used to calculate the membrane deflection w_{max}. In parallel, the membrane was optically characterized, flat or deformed by the actuating magnet. Experimental optical patterns were fitted by the optical model (eqn (7)–(8)), with the following input parameter: laser wavelength and spot location on the membrane, membrane size and distance from the screen, embedded grating dimensions, and the unknown geometrical deflection w_{max} characterizing the deformed membrane concavity. A precise fit of our optical model with the experimental optical patterns, by adjusting the parameter w_{max}, yielded the experimental deter-

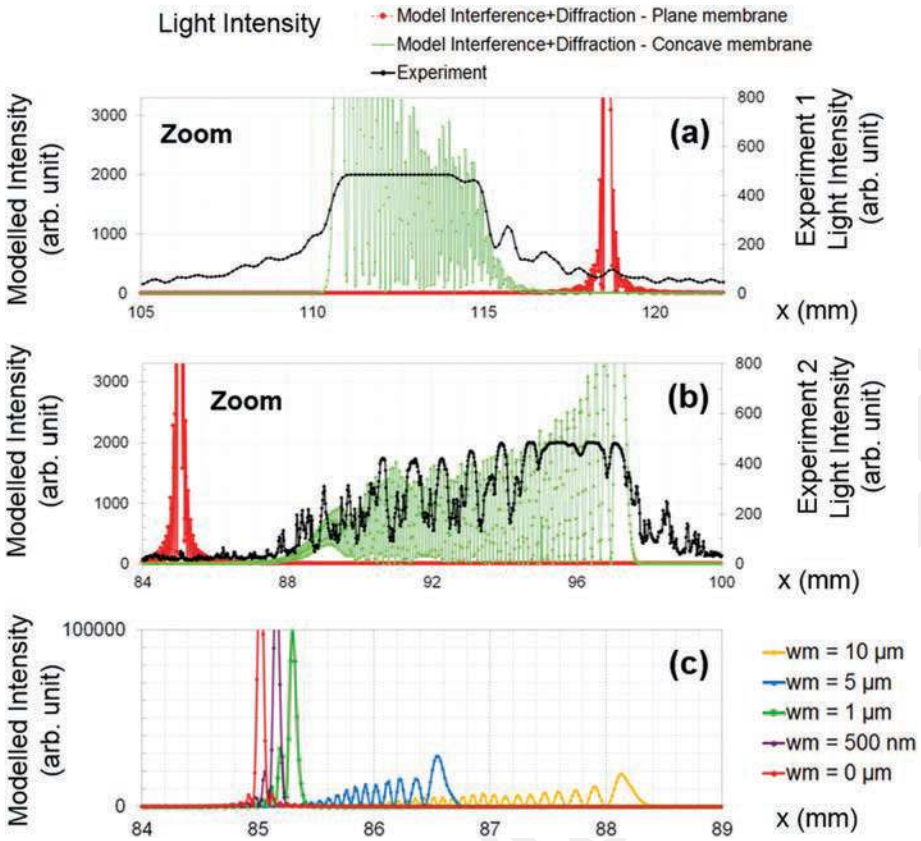

Fig. 10 Optics. Experiment and optical model, zoomed around the interference order m = 0. (a–b) Zooms of the light profiles presented in Fig. 9. (a) Experiment 1 + optical model, (b) experiment 2 + optical model, (c) extrapolation of the light intensity on the screen: model only, along the OX axis around the interference peak of order m = 0, for small membrane concavities: w_{max} = 0 (planar); 500 nm; 1 µm; 5 µm; 10 µm.

mination of the deflection w_{max}. A very good agreement was then obtained between the deflection calculated by the magneto-elastic model and the one determined from the optical experiments, thus confirming the validity of the various models.

Conclusion

The optical response of the magneto-elastic membrane (MEM) actuated by a magnetic field was experimentally characterized and fitted by a magneto-mechanical and optical model. Based on the magnetic properties of the membrane and magnet, and adopting an elastic plate model, the resulting membrane deflection w_{max} led to the expected diffraction/interference patterns. The membrane concavity and its impact on the optical signal transformation were quantified.

To achieve this, the magneto-elastic membrane presented here was first fabricated. It comprises arrays of magnetic particles of various geometries deposited on a PDMS membrane coated with a 100 nm thick Au layer. The PDMS membrane played here the role of a protective transparent layer, required for the membrane resilience and a potential biocompatibility. However, the 100 nm Au layer determined the membrane deflection amplitude. Further studies will aim at suppressing or at least thinning this Au layer, by adapting the technique of magnetic material deposition, for fabricating either Au/PDMS bilayers, or PDMS monolayers, presenting the lower and tunable Young's modulus of the PDMS instead of the gold's modulus.

The MEM was then characterized – magnetic and mechanical properties explored – and tested in magnetic fields by optical experiments. The magnetic properties of the embedded arrays of permalloy cylinders were measured and modelled, revealing the probable presence of magnetic vortex states. Membrane actuation by the applied magnetic field was precisely measured and modelled. The resulting micrometric membrane deformations were calculated using a "clamped plate" mechanical model. The MEM can be viewed as an actuable diffraction grating. The resulting diffraction patterns were characterized, and correlated to the expected patterns for two-dimensional (2D) periodic arrays. A very strong optical response to the magnetic field was demonstrated, especially when the membrane is used in reflection. Indeed, the transmitted pattern remains almost unchanged, while the reflected patterns present largely extended interference fringes when the membrane is actuated. Such optical responses have been quantitatively correlated with the membrane structure. Firstly,

the optical model takes into account the membrane concavity influence on the reflected light intensity. Then, the analytical magneto-mechanical models are used for the input parameters in optics. This magneto-mechanical modelling turned out to be quantitatively pertinent when used in the final modelling of the membrane optical response. As an order of magnitude, the diffraction patterns of a membrane of diameter 0.8 cm can be significantly impacted by membrane deformations in micro- and nanoscale ranges, from <50 μm down to about a few hundred nm.

The optical properties of these magneto-elastic membranes can be further explored, and the study of their optical response to the magnetic actuation deepened. Finally, such a field-controlled optical response, especially in reflection, may be used in optical applications, photonic devices, and for biological applications, where the membrane deformations can be used to stimulate biological reactions on biological species.

Conflicts of interest

There are no conflicts to declare.

Acknowledgements

This work has been supported by funding from the European Union's Horizon 2020 research and innovation programme under grant agreement No 665440.

References

1 H. Watson, *Essays Biochem.*, 2015, **59**, 43–69.
2 D. Carugo, M. Aron, E. Sezgin, J. B. de la Serna, M. K. Kuimova, C. Eggeling and E. Stride, *Biomaterials*, 2017, **113**, 105–117.
3 R. N. Palchesko, L. Zhang, Y. Sun and A. W. Feinberg, *PLoS One*, 2012, **7**, e51499.
4 A. Alrifaiy, O. A. Lindahl and K. Ramser, *Polymers*, 2012, **4**, 1349–1398.
5 A. Mata, A. J. Fleischman and S. Roy, *Biomed. Microdevices*, 2005, **7**, 281–293.
6 J. L. Wilbur, R. J. Jackman, G. M. Whitesides, E. L. Cheung, L. K. Lee and M. G. Prentiss, *Chem. Mater.*, 1996, **8**, 1380–1385.
7 K. Raman, T. R. Srinivasa Murthy and G. M. Hegde, *Phys. Procedia*, 2011, **19**, 146–151.
8 S. Walia, C. M. Shah, P. Gutruf, H. Nili, D. R. Chowdhury, W. Withayachumnankul, M. Bhaskaran and S. Sriram, *Appl. Phys. Rev.*, 2015, **2**, 1–14.
9 D. Huh, B. D. Matthews, A. Mammoto, M. Montoya-Zavala, H. Y. Hsin and D. E. Ingber, *Science*, 2010, **328**, 1662–1668.
10 T. Fujii, *Microelectron. Eng.*, 2002, **61–62**, 907–914.
11 B. D. Iverson and S. V. Garimella, *Microfluid. Nanofluid.*, 2008, **5**, 145–174.
12 J. J. Kim, S. E. Chung, S. E. Choi, H. Lee, J. J. Kim and S. Kwon, *Nat. Mater.*, 2011, **10**, 747–752.
13 Z. Z. Chong, W. J. Sim, Z. T. Yeo, K. H. Li, S. H. Ng, H. Xia, T. N. Wong, N. H. Loh, S. B. Tor, S. H. Tan and N.-T. Nguyen, *Micro Nanosyst.*, 2014, **6**, 232–236.
14 M. Khoo and C. Liu, *Sens. Actuators, A*, 2001, **89**, 259–266.
15 J. Le Digabel, N. Biais, J. Fresnais, J. F. Berret, P. Hersen and B. Ladoux, *Lab Chip*, 2011, **11**, 2630–2636.
16 M. Shen, L. Dovat and M. A. M. Gijs, *Sens. Actuators, B*, 2011, **154**, 52–58.
17 F. Pirmoradi, L. Cheng and M. Chiao, *J. Micromech. Microeng.*, 2010, **20**, 7.
18 M. Khoo and C. Liu, Proc. 22nd Annu. Int. Conf. IEEE Eng. Med. Biol. Soc. (Cat. No.00CH37143), 2000, vol. 3, pp. 4–7.
19 S. M. Yusuf, K. R. Balakrishnan and J. V. Yakhmi, *US* 2012/0323318A1, 2012, US 2012/03.
20 C. A. Grimes, *IEEE Trans. Biomed. Eng.*, 1995, **31**, 4109–4111.
21 J. Rittinger, P. Taptimthong, L. Jogschies, M. C. Wurz and L. Rissing, in Proc. of SPIE Smart Sensors, Actuators, and MEMS VII; and Cyber Physical Systems, 2015, pp. 1–9.
22 E. Fernández, G. V. Kurlyandskaya, A. García-arribas and A. V. Svalov, *Nanoscale Res. Lett.*, 2012, **7**, 1–5.
23 K. Agra, T. J. A. Mori, L. S. Dorneles, V. M. Escobar, U. C. Silva, C. Chesman, F. Bohn and M. A. Corrêa, *J. Magn. Magn. Mater.*, 2014, **355**, 136–141.
24 L. M. Sanchez, V. A. Alvarez and J. S. Gonzalez, in *Handbook of Composites from Renewable Materials, Vol 8: Nanocomposites: Adv. Appl. Chap. 21: Ferrogels: smart materials for biomedical and remediation applications*, ed. V. K. Thakur, M. K. Thakur and M. R. Kessler, John Wiley & Sons, 2017, pp. 561–579.
25 R. Weeber, S. Kantorovich and C. Holm, *J. Chem. Phys.*, 2015, **143**, 1–11.
26 A. Shankar, A. P. Safronov, E. A. Mikhnevich, I. V. Beketov and G. V. Kurlyandskaya, *Soft Matter*, 2017, **13**, 3359–3372.
27 M. Zrinyi, L. Barsi and A. Büki, *Polym. Gels Networks*, 1997, **5**, 415–427.
28 G. V. Kurlyandskaya, I. P. Novoselova, V. V. Schupletsova, R. Andrade, N. A. Dunec, L. S. Litvinova, A. P. Safronov, K. A. Yurova, N. A. Kulesh, A. N. Dzyuman and I. A. Khlusov, *J. Magn. Magn. Mater.*, 2017, **431**, 249–254.
29 E. Zhang, M. F. Kircher, X. M. Koch, L. Eliasson and S. N. Goldberg, *ACS Nano*, 2014, **8**, 3192–3201.
30 S. Leulmi, X. Chauchet, M. Morcrette, G. Ortiz, H. Joisten, P. Sabon, T. Livache, Y. Hou, M. Carrière, S. Lequien and B. Dieny, *Nanoscale*, 2015, **7**, 15904–15914.
31 D.-H. Kim, E. A. Rozhkova, I. V. Ulasov, S. D. Bader, T. Rajh, M. S. Lesniak and V. Novosad, *Nat. Mater.*, 2010, **9**, 165–171.
32 M. P. Nikitin, A. V. Orlov, I. L. Sokolov, A. A. Minakov, P. I. Nikitin, J. Ding, S. D. Bader, E. A. Rozhkova and V. Novosad, *Nanoscale*, 2018, **10**, 11642–11650.
33 Y. Cheng, M. E. Muroski, D. C. M. C. Petit, R. Mansell, T. Vemulkar, R. A. Morshed, Y. Han, I. V. Balyasnikova, C. M. Horbinski, X. Huang, L. Zhang, R. P. Cowburn and M. S. Lesniak, *J. Controlled Release*, 2016, **223**, 75–84.

34 C. Levartoski De Araujo, S. Alves, L. Buda-prejbeanu and B. Dieny, *Phys. Rev. Appl.*, 2016, **6**, 1–9.
35 C. Li, L. Cai, B. Liu, X. Yang, H. Cui, S. Wang and B. Wei, *AIP Adv.*, 2018, **8**, 1–5.
36 M. T. Bryan, S. R. Shelley, M. J. Parish, P. G. Petrov, C. P. Winlove, A. D. Gilbert and F. Y. Ogrin, *J. Appl. Phys.*, 2017, **121**, 1–6.
37 J. K. Hamilton, P. G. Petrov, C. P. Winlove, A. D. Gilbert, M. T. Bryan and F. Y. Ogrin, *Sci. Rep.*, 2017, **7**, 1–7.
38 J. K. Hamilton, M. T. Bryan, A. D. Gilbert, F. Y. Ogrin and T. O. Myers, *Sci. Rep.*, 2018, **8**, 1–12.
39 C. Iss, G. Ortiz, A. Truong, Y. Hou, T. Livache, R. Calemczuk, P. Sabon, E. Gautier, S. Auffret, L. D. Buda-Prejbeanu, N. Strelkov, H. Joisten and B. Dieny, *Sci. Rep.*, 2017, **7**, 1–9.
40 C. M. Bidan, M. Fratzl, A. Coullomb, P. Moreau, A. H. Lombard, I. Wang, M. Balland, T. Boudou, N. M. Dempsey, T. Devillers and A. Dupont, *Sci. Rep.*, 2018, **8**, 1–13.
41 R. Davies and M. Kasper, *Annu. Rev. Astron. Astrophys.*, 2012, **1056–8700**, 1–47.
42 M. Stürmer, M. C. Wapler, J. Schmitt, F. Völklein and U. Wallrabe, *Opt. Express*, 2016, **24**, 23765.
43 G. Ouyang, K. Wang, L. Henriksen, M. N. Akram and X. Y. Chen, *Sens. Actuators, A*, 2010, **158**, 313–319.
44 K. Hosokawa, K. Hanada and R. Maeda, *J. Micromech. Microeng.*, 2002, **12**, 1–6.
45 Z. Xu, X. Wang, K. Han, S. Li and G. L. Liu, *J. Opt. Soc. Am. A*, 2013, **30**, 2466.
46 W. Song, A. E. Vasdekis and D. Psaltis, *Lab Chip*, 2012, **12**, 3590–3597.
47 R. Gu, M. Ji, Y. Xuan, Y. Cui, C. Yuan, W. Di Li, H. Ge and Y. Chen, *Appl. Phys. A: Mater. Sci. Process.*, 2015, **121**, 335–341.
48 G. England, M. Kolle, P. Kim, M. Khan, P. Munoz, E. Mazur and J. Aizenberg, *Proc. Natl. Acad. Sci. U. S. A.*, 2014, **111**, 15630–15634.
49 A. Truong, G. Ortiz, M. Morcrette, T. Dietsch, P. Sabon, I. Joumard, A. Marty, H. Joisten and B. Dieny, *Sci. Rep.*, 2016, **6**, 1–8.
50 H. Lu and J. Zhu, in Australasian Universities Power Engineering Conf. (AUPEC 2004) 26–29 Sept., Brisbane, Australia, 2004, pp. 26–29.
51 A. M. Alneamy, M. Khater, S. Park, E. M. Abdel-Rahman and G. R. Heppler, in XXIV ICTAM, Montreal, Canada, 2016, pp. 1–2.
52 D. K.-C. Liu, J. Friend and L. Yeo, *Acoust. Sci. Technol.*, 2010, **31**, 115–123.
53 O. Cugat, J. Delamare and G. Reyne, *IEEE Trans. Magn.*, 2003, **39**, 3607–3612.
54 W. Zhang, H. Yan, Z. Peng and G. Meng, *Sens. Actuators, A*, 2014, **214**, 187–218.
55 D. Niarchos, *Sens. Actuators, A*, 2003, **109**, 166–173.
56 E. J. Fernández, L. Vabre, B. Hermann, A. Unterhuber, B. Považay and W. Drexler, *Opt. Express*, 2006, **14**, 8900–8917.
57 O. Cugat, S. Basrour, C. Divoux, P. Mounaix and G. Reyne, *Sens. Actuators, A*, 2001, **89**, 1–9.
58 H. Ren and S.-T. Wu, *Appl. Sci.*, 2018, **8**, 1–15.
59 L. Dong, A. K. Agarwal, D. J. Beebe and H. Jiang, *Nature*, 2006, **442**, 551–554.
60 H. Cheng, S. Xu, Y. Liu, S. Levi and S. Wu, *Opt. Commun.*, 2011, **284**, 2118–2121.
61 F. Carpi, G. Frediani, S. Turco and D. De Rossi, *Adv. Funct. Mater.*, 2011, **21**, 4152–4158.
62 M. Zenger, W. Breuer, M. Zölfl, R. Pulwey, J. Raabe and D. Weiss, *IEEE Trans. Magn.*, 2001, **37**, 2094–2097.
63 J. I. Martín, J. Nogués, K. Liu, J. L. Vicent and I. K. Schuller, *J. Magn. Magn. Mater.*, 2003, **256**, 449–501.
64 S. Petit, C. Baraduc, C. Thirion, U. Ebels, Y. Liu, M. Li, P. Wang and B. Dieny, *Phys. Rev. Lett.*, 2007, **98**, 1–4.
65 A. Bollero, L. D. Buda-Prejbeanu, V. Baltz, B. Rodmacq and B. Dieny, *IEEE Trans. Magn.*, 2006, **42**, 2990–2992.
66 A. V. Bodnaruk, A. Brunhuber, V. M. Kalita, M. M. Kulyk, A. A. Snarskii, A. F. Lozenko, S. M. Ryabchenko and M. Shamonin, *J. Appl. Phys.*, 2018, **123**, 1–7.
67 S. Leulmi, H. Joisten, T. Dietsch, C. Iss, M. Morcrette, S. Auffret, P. Sabon and B. Dieny, *Appl. Phys. Lett.*, 2013, **103**, 1–5.
68 K. Y. Guslienko, V. Novosad, Y. Otani, H. Shima and K. Fukamichi, *Appl. Phys. Lett.*, 2001, **78**, 3848–3850.
69 L. F. Yin, D. H. Wei, N. Lei, L. H. Zhou, C. S. Tian, G. S. Dong and X. F. Jin, *Phys. Rev. Lett.*, 2006, **97**, 1–4.
70 A. Garcıa-Arribas, E. Fernandez, A. V. Svalov, G. V. Kurlyandskaya, A. Barrainkua, D. Navas and J. M. Barandiaran, *Eur. Phys. J. B*, 2013, **86**, 1–7.
71 R. D. Gomez, T. V. Luu, A. O. Pak, K. J. Kirk and J. N. Chapman, *J. Appl. Phys.*, 1999, **85**, 6163–6165.
72 A. Hirohata, H. T. Leung, Y. B. Xu, C. C. Yao, W. Y. Lee, J. A. C. Bland and S. N. Holmes, *IEEE Trans. Magn.*, 1999, **35**, 3886–3888.
73 K. L. Metlov and K. Y. Guslienko, *J. Magn. Magn. Mater.*, 2002, **242–245**, 1015–1017.
74 K. L. Metlov and Y. Lee, *Appl. Phys. Lett.*, 2008, **92**, 1–3.
75 K. L. Metlov, *J. Appl. Phys.*, 2013, **113**, 1–5.
76 M. F. Lai, C. R. Chang, J. C. Wu, Z. H. Wei, J. H. Kuo and J. Y. Lai, *IEEE Trans. Magn.*, 2002, **38**, 2550–2552.
77 N. Kikuchi, S. Okamoto, O. Kitakami, Y. Shimada, S. G. Kim, Y. Otani and K. Fukamichi, *IEEE Trans. Magn.*, 2001, **37**, 2082–2084.
78 C. A. Ross, M. Hwang, M. Shima, J. Y. Cheng, M. Farhoud, T. A. Savas, H. I. Smith, W. Schwarzacher, F. M. Ross, M. Redjdal and F. B. Humphrey, *Phys. Rev. B: Condens. Matter Mater. Phys.*, 2002, **65**, 1–8.
79 S. Timoshenko and S. Woinowsky-Krieger, *Theory of Plates and Shells*, 2nd edn, 1959.
80 Y. Zhang, *Sci. China: Phys., Mech. Astron.*, 2016, **59**, 1–11.
81 C. A. Rothenbach, I. I. Kravchenko and M. C. Gupta, *Appl. Opt.*, 2015, **54**, 1808–1818.
82 Ibsen Photonics, http://spectrometerguide.com/tutorials/spectrometer/diffraction-grating/.
83 M. Born and E. Wolf, *Principles of Optics*, Cambridge University Press, 1959.